

Marquette University

e-Publications@Marquette

Master's Theses (2009 -)

Dissertations, Theses, and Professional
Projects

Simulation of Power Control of a Wind Turbine Permanent Magnet Synchronous Generator System

Nantao Huang
Marquette University

Follow this and additional works at: https://epublications.marquette.edu/theses_open



Part of the [Power and Energy Commons](#)

Recommended Citation

Huang, Nantao, "Simulation of Power Control of a Wind Turbine Permanent Magnet Synchronous Generator System" (2013). *Master's Theses (2009 -)*. 215.
https://epublications.marquette.edu/theses_open/215

SIMULATION OF POWER CONTROL OF A WIND TURBINE PERMANENT
MAGNET SYNCHRONOUS GENERATOR SYSTEM

by
Nantao Huang, B.S.

A Thesis submitted to the Faculty of the Graduate School,
Marquette University,
in Partial Fulfillment of the Requirements for
the Degree of Master of Science

Milwaukee, Wisconsin

August 2013

ABSTRACT

SIMULATION OF POWER CONTROL OF A WIND TURBINE PERMANENT MAGNET SYNCHRONOUS GENERATOR SYSTEM

Nantao Huang, B.S.

Marquette University, 2013

This thesis presents a control system for a 2MW direct-drive permanent magnet synchronous generator wind turbine system with the objectives to capture the optimal power from the wind and ensure a maximum efficiency for this system. Moreover, in order to eliminate the electrical speed sensor mounted on the rotor shaft of the PMSG to reduce the system hardware complexity and improve the reliability of the system, a sliding mode observer based PM rotor position and speed sensorless control algorithm is presented here.

The mathematical models for the wind turbine and the permanent magnet synchronous machine are first given in this thesis, and then optimal power control algorithms for this system are presented. The optimal tip speed ratio based maximum power point tracking control is utilized to ensure the maximum power capture for the system. The field oriented control algorithm is applied to control the speed of the PMSG with the reference of the wind speed. In the grid-side converter control, voltage oriented control algorithm is applied to regulate the active and reactive power injected into the power grid. What is more, sliding mode observer based sensorless control algorithm is also presented here. The simulation study is carried out based on MATLAB/Simulink to validate the proposed system control algorithms.

TABLE OF CONTENTS

TABLE OF CONTENTS.....	i
LIST OF TABLES.....	iii
LIST OF FIGURES.....	iv
CHAPTER	
1. INTRODUCTION.....	1
1.1 Background.....	1
1.2 Literature Review.....	5
1.2.1 Power Converters for WECSs.....	5
1.2.2 Rotor Speed and Position Sensorless Control.....	11
1.3 Thesis Contribution and Organization.....	14
2. MODELING AND ANALYSIS OF THE DIRECT-DRIVE PERMANENT MAGNET SYNCHRONOUS GENERATOR WIND TURBINE SYSTEMS.....	16
2.1 Modeling of Wind Turbines.....	16
2.2 Modeling of Permanent Magnet Synchronous Machines.....	21
2.2.1 Modeling of a PMSM in the natural abc three-phase stationary reference frame.....	21
2.2.2 Modeling of the PMSG in the d-q reference frame.....	23
2.2.3 Power and torque analysis of a PMSM.....	25
3. CONTROL OF GENERATOR-SIDE CONVERTER.....	27
3.1 Maximum Power Point Tracking Control.....	28
3.2 Comparison between Direct Torque Control and Field Oriented Control.....	31
3.3 Field Oriented Control based Generator-Side Converter Control.....	33
3.4 Simulation Results and Analysis.....	35
4. CONTROL OF GRID-SIDE CONVERTER.....	49

4.1 Grid-Side Converter Control based on Voltage Oriented Control.....	49
4.2 Space Vector Pulse Width Modulation.....	52
4.2.1 Switching States.....	53
4.2.2 Space Vectors.....	56
4.2.3 Implementation of SVPWM.....	58
4.3 Simulation Results and Analysis.....	64
5. Sliding Mode Observer based Rotor Position and Speed Sensorless Control.....	70
5.1 Sliding Mode Control.....	70
5.2 Simulation Results and Analysis.....	76
6. Conclusions and Future Works.....	80
6.1 Conclusions.....	80
6.2 Future Work.....	81
REFERENCES.....	82

LIST OF TABLES

Table 3.1 Parameters and operating conditions of the generator side control system.....	36
Table 4.1 Switching states and output voltages of the VSI.....	55
Table 4.2 VSI phase voltage space vectors in different switching states.....	57
Table 4.3 Determination of the location of the reference voltage space vector.....	61
Table 4.4 Seven segments switching sequence.....	64

LIST OF FIGURES

Figure 1.1 Global cumulative wind power capacity.....	2
Figure 1.2 System configuration of the direct-drive wind generation system.....	4
Figure 1.3 DFIG with partial-scale power converters.....	6
Figure 1.4 Wind turbine generators with full-scale power converters.....	6
Figure 1.5 Two-level back-to-back converters with passive rectifier.....	7
Figure 1.6 Two-level back-to-back converters with active rectifier.....	7
Figure 1.7 Two-level VSC with series-connected power switches.....	8
Figure 1.8 Multi-pulse diode rectifier circuit configuration and input current: (a) 12 pulse, (b) 18 pulse, and (c) 24 pulse.....	9
Figure 1.9 The NPC converter.....	10
Figure 1.10 CHB power cells	11
Figure 2.1 Blade angle schematic diagram.....	20
Figure 2.2 Cross-section view of the PMSM.....	22
Figure 2.3 The dq -axes equivalent circuits of a PMSM.....	25
Figure 3.1 Direct-drive PMSG system.....	27
Figure 3.2 Wind turbine power-speed characteristics.....	28
Figure 3.3 Power coefficient characteristics.....	30
Figure 3.4 Tip speed ratio control scheme.....	31
Figure 3.5 Phasor diagram of the FOC.....	34
Figure 3.6 Generator-side control scheme.....	34
Figure 3.7 Control diagram of the system.....	37
Figure 3.8 Control diagram of the FOC approach.....	38
Figure 3.9 Wind speed input for the wind power generation system.....	40

Figure 3.10 Actual electrical angular speed of the PMSG.....	40
Figure 3.11 Three-phase stator currents of the PMSG.....	41
Figure 3.12 d -axis current of the PMSG.....	41
Figure 3.13 q -axis current of the PMSG.....	42
Figure 3.14 Electromagnetic torque developed by the PMSG.....	42
Figure 3.15 Electrical power generated by the PMSG.....	43
Figure 3.16 System Parameters in Static States with Wind Speed of $8m/s$	46
Figure 3.17 System parameters in static states with wind speed of $13m/s$	47
Figure 4.1 Simplified topology of the direct-drive PMSG wind generation system.....	50
Figure 4.2 Phasor diagram of the VOC.....	51
Figure 4.3 Control scheme of the grid-side converter.....	52
Figure 4.4 Two level voltage source inverter.....	54
Figure 4.5 Voltage space vector diagram for the two level VSI.....	58
Figure 4.6 Dwell time calculation diagram when the reference voltage vector is in sector I.....	61
Figure 4.7 Seven-segment switching sequence of the SVPWM for sector I.....	63
Figure 4.8 Control scheme of the grid-side converter.....	66
Figure 4.9 Grid voltages of the system.....	67
Figure 4.10 Grid currents of the system.....	67
Figure 4.11 The d -axis component of the grid current.....	68
Figure 4.12 The q -axis component of the grid current.....	68
Figure 4.13 The active and reactive power injected into the grid.....	69
Figure 5.1 Operation properties of the signum function.....	72
Figure 5.2 Block diagram of the sliding mode observer.....	75
Figure 5.3 Control scheme of the wind turbine generation system including the sliding mode observer.....	76
Figure 5.4 Estimated and actual rotor speed.....	77

Figure 5.5 Estimated and actual rotor speed (wind speed=8m/s).....	77
Figure 5.6 Estimated and actual rotor speed (wind speed=13m/s).....	78
Figure 5.7 Estimated and actual rotor position angle.....	78

Chapter 1: Introduction

1.1 Background

Electrical and hybrid vehicles, which are considered as the best replacement of conventional fossil fuel internal combustion engine based vehicles, have been greatly evolving and significantly commercialized during the recent years. Accordingly, there will be a growing demand for electrical energy when these vehicles become part of the electric grid load. Conventional electrical energy sources depend heavily on fossil fuels burning. However, burning of the fossil fuels causes environmental issues such as global warming, acid rain and urban smog, etc. by releasing carbon dioxide, sulfur dioxide, and other pollutants into the atmosphere [1]. Based on the issue, the renewable energy, which includes photovoltaic energy, wind energy, and geothermal energy, etc., has been heavily investigated and rapidly developing [2]. Renewable energy has the advantages that it is abundant, clean, and becoming increasingly economical. In fact, renewable energy sources help in reducing about 70 million metric tons of carbon emissions per year that would have been produced by fossil fuels [3]. Among various types of renewable energy sources, wind energy is one of the fastest growing renewable energy sources [4]. Shown in Figure 1.1 is a histogram of the global cumulative wind power capacity from 1996 to 2011. As can be seen in this figure, the global cumulative wind power capacity has been explosively increased from about 6.1 GW in 1996 to 238.4 GW in 2011, and the growth rate is expected to continue in the coming years.

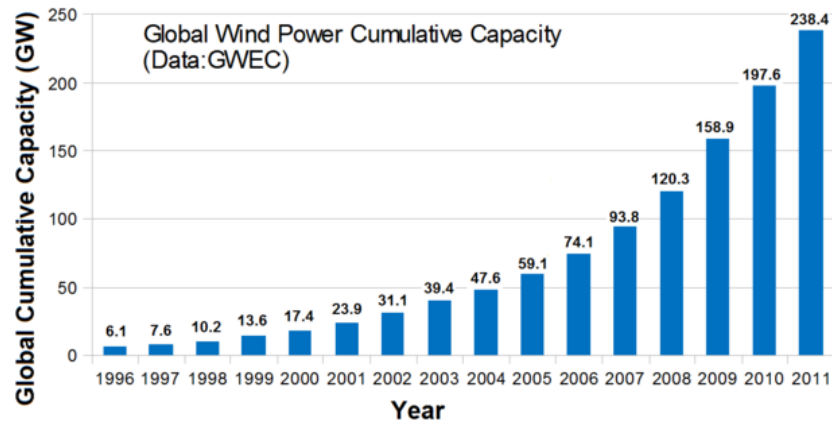


Figure 1.1 Global cumulative wind power capacity [5]

In wind energy conversion systems (WECSs), the key technologies include wind turbine technology, power electronics technology, and system control technology. For the wind turbines, based on the orientation of the rotation axis of the wind turbine, there are horizontal-axis wind turbines and vertical-axis wind turbines [6]. In the horizontal-axis wind turbines, the rotation axis of the wind turbine is parallel to the ground, while in the vertical-axis wind turbines, the rotation axis is perpendicular to the ground. Compared to the vertical-axis wind turbines, horizontal-axis wind turbines have higher wind energy conversion efficiency, which are widely applied in the wind energy industry. The wind turbines can also be classified as fixed-speed wind turbines and variable-speed wind turbines based on whether the operation speed is controllable. The fixed-speed wind turbines possess the merits that they are simple, robust, and require lower construction and maintenance cost. However, their operation speed is fixed and cannot be controlled with the variation of the wind speed, which results in lower energy conversion efficiency compared to the variable-speed wind turbines. Nowadays, most of the wind turbines

applied in industry are variable-speed wind turbines. Among various types of variable-speed WECSs, three kinds are most widely applied in industry: (1) doubly-fed induction generator (DFIG) WECSs with reduced-capacity power converters, (2) geared/gearless squirrel-cage induction generator (SCIG) WECSs with full-capacity power converters, and (3) geared/gearless wound-rotor synchronous generator (WRSG)/permanent magnet synchronous generator (PMSG) WECSs with full-capacity power converters [6]. In the DFIG WECSs, only 30% of the rated power is processed by the power converters, which greatly reduces the cost of the converters while preserving the capability to control the speed of the generator in the range of about $\pm 30\%$ of its rated speed [6]. In SCIG, WRSG and PMSG WECSs, full-capacity power converters are needed to process the power generated by the generators up to the rated power of the systems. With the application of the full-capacity power converters, the generators are fully decoupled from the grid, and are able to operate in the full speed range. As the large scale wind turbines (up to 10 MW) attract more and more attention nowadays, the direct-drive PMSG based WECSs which are very suitable for large scale wind plants have become a "hot topic". In this thesis, the control algorithms for the direct-drive wind turbine PMSG systems are studied and simulated. The direct-drive wind turbine PMSGs do not have the gearbox between the wind turbine and the PMSG rotor shaft, which avoids the mechanical power losses caused by the gearbox. Moreover, the removal of the gearbox also helps in reducing the cost of the system. The overall configuration of a direct-drive wind turbine PMSG system is shown in Figure 1.2. As can be seen in this figure, this system is composed of a wind turbine PMSG, a rectifier, and an inverter. The wind turbine PMSG transforms the mechanical power from the wind into the electrical power, while the

rectifier converts the AC power into DC power and controls the speed of the PMSG. The controllable inverter helps in converting the DC power to variable frequency and magnitude AC power. With the voltage oriented control algorithm, the inverter also possesses the ability to control the active and reactive powers injected into the grid.

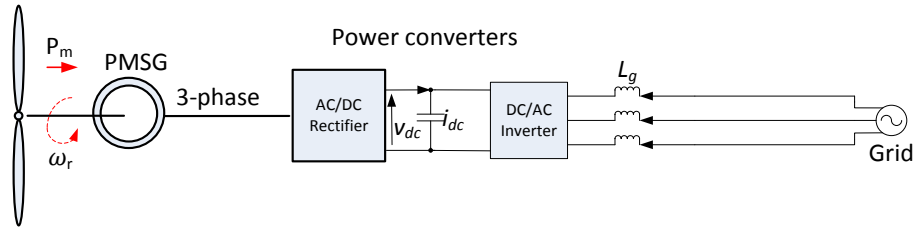


Figure 1.2 System configuration of the direct-drive wind generation system

For the control of direct-drive PMSG systems, the information of the rotor position and speed is needed to implement the advanced control algorithms such as the field oriented control (FOC) and direct torque control (DTC). Conventional methods to acquire the rotor position and speed information are based on an encoder or a transducer mounted on the rotor shaft. However, such electrical speed sensors increase the hardware complexity and system cost. In addition, the rotor mounted sensors have to endure the constant oscillations of the rotor shaft, which reduces the reliability of the system. According to [7], speed sensor failures cause more than 14% of failures in such WECSs. The malfunction of the speed sensor will cause the breakdown of the whole system, which will contribute to considerable losses in power production. Moreover, the repair of the failed components results in additional cost. Based on this issue, this thesis proposes a

back EMF based rotor position and speed sensorless control algorithm, which will be analyzed later.

1.2 Literature Review

In this section, the literature review on the state of the art of power converters for different types of WECSs will be made. Moreover, several important rotor position and speed sensorless control algorithms that have been previously investigated and published will be reviewed.

1.2.1 Power Converters for WECSs

Power electronics devices have been applied in WECSs since the 1980s, when a thyristor based soft-starter was applied to a SCIG system which was directly connected to the grid [8]. The thyristor based soft-starter was used for limiting the current surge during start up. In the 1990s, the emergence of the rotor resistance control approach made it possible that the WRSG can be controlled to operate at variable speed. Although the speed range is only limited to 10% above the synchronous speed of the generator, this progress has improved the energy capture efficiency of the wind turbine due to the application of the converter controlled variable resistance. Nowadays, back-to-back converters are widely used in WECSs, either in reduced power (reduced power means that only the 30% of the rated power is processed by the power converters) for DFIG systems shown in Figure 1.3, or in full power (full power means that the power generated by the generator up to its rated power is processed by the power converters) for PMSG/SCIG/WRSG systems which can be seen in Figure 1.4.

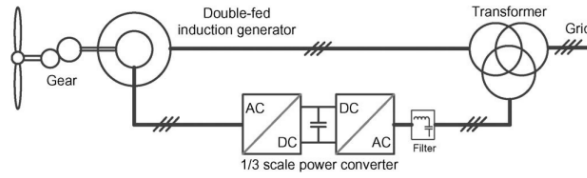


Figure 1.3 DFIG with partial-scale power converters [8]

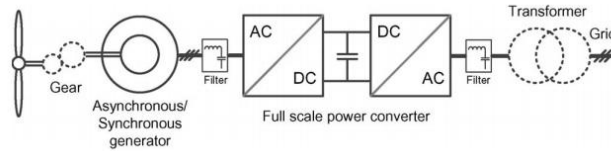


Figure 1.4 Wind turbine generators with full-scale power converters [8]

The back-to-back power converters, which decouple the wind turbine from the grid, possess the capability to regulate the operation speed of such wind turbine generators, control the active and reactive powers injected into the grid, and improve the power quality. Conventional two-level back-to-back power converters have been widely applied in wind power industry and their reliability has been well proved. With the development of the semiconductor devices and the digital control technology, multilevel converters were investigated and commercialized during recent years, which helps in improving the power level and the power quality of the wind energy generation systems.

The most widely applied power converters for the best seller range 1.5-3.0 MW WECSs are the two-level back-to-back voltage source converters (VSCs) [9]. Figure 1.5 and 1.6 are showing two typical two-level back-to-back VSCs.

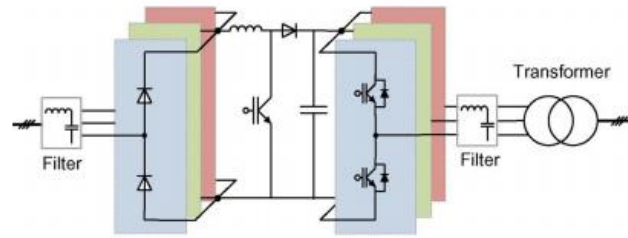


Figure 1.5 Two-level back-to-back converters with passive rectifier [8]

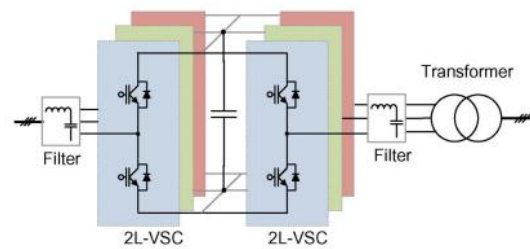


Figure 1.6 Two-level back-to-back converters with active rectifier [8]

Shown in Figure 1.5 is a two-level back-to-back converter with a passive diode rectifier and a DC chopper. Figure 1.6 shows a two-level back-to-back converter with an active rectifier, as well as an active inverter connected to the grid. As can be seen in Figure 1.5 and 1.6, the insulated gate bipolar transistors (IGBTs) are used as the power switches. Although recent developments have made the IGBT with higher-voltage blocking capability closer to the integrated gate-commutated thyristor (IGCT), the IGBT based two-level back-to-back VSCs are applied mainly in the low-voltage, low/medium-power drive industries [10]. As introduced in [11], to increase the voltage level, as well as the power level of the conventional two-level back-to-back VSCs, series-connected power switches can be applied as shown in Figure 1.7. Based on this topology of power

switches connection, the series connected IGBTs distribute the voltage and power stress on the single IGBT in the conventional two-level VSCs, which improves the voltage and power level of the two-level VSCs. With the application of the series-connected IGBT two-level high power inverters, the multi-pulse rectifiers become attractive selections for the high power back-to-back VSCs. These types of rectifiers help in reducing the input current harmonics which is beneficial for the generators in wind turbine systems. Figure 1.8 shows the 12, 18, and 24 pulse rectifier circuit configurations.

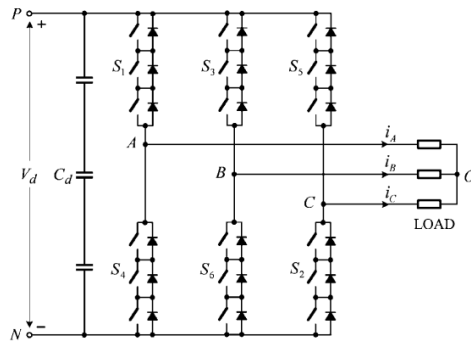


Figure 1.7 Two-level VSC with series-connected power switches [11]

Although the series-connected IGBT VSC has greatly improved the voltage and power level of the two-level VSC, it contributes nothing to reduce the dv/dt (the voltage change, dv , within the time interval, dt), or to improve the power quality [10]. Based on this concern, the multilevel converters were investigated and commercialized. Among various types of multilevel converters, the neutral-point clamped (NPC) converters, cascaded H-bridge (CHB) converters, flying capacitor converters, and Active NPC converters are the most studied ones. Here, the research on NPC and CHB converters which are the most widely applied types of multilevel converters will be reviewed.

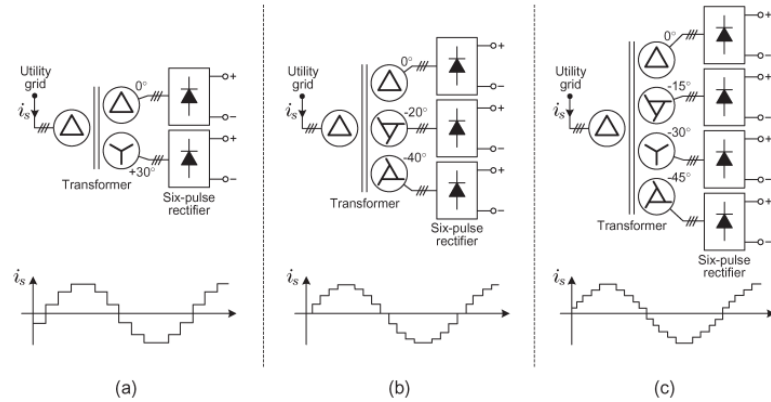


Figure 1.8 Multi-pulse diode rectifier circuit configuration and input current: (a) 12 pulse, (b) 18 pulse, and (c) 24 pulse [10]

A. Neutral-Point Clamped Multilevel Converters

The NPC multilevel converter was proposed in [12] [13] in the early 1980s. It can be structured as three level, five level, and even seven level or more. However, the three-level NPC converter is the most applied type in industry. In each leg of the three-level NPC converter, there are four power switches which are clamped with diodes to a midpoint of the capacitor bank as shown in Figure 1.9. To this converter, all conventional pulse width modulation (PWM) approaches are applicable [12]. Since the commutation voltage of all the power switches in the NPC converter is only half of the DC bus voltage, the NPC converter is very suitable for the high power, medium voltage drives (2.3-4.16 kV) [11]. What is more, since the conduction of the power switches only shares half of the DC bus voltage, the dv/dt is greatly reduced. The output line-to-line voltages of the NPC converter consists of three voltage levels, which result in reduced harmonics in the output voltages and improved power quality. The main drawback of the NPC converter is

that the power losses on the power switches are unevenly distributed, which reduces the reliability of the NPC converters [14].

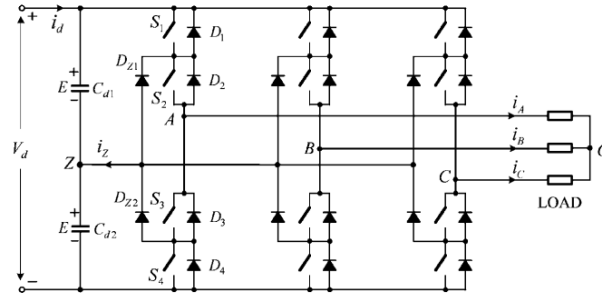


Figure 1.9 Topology of the NPC converter [17]

B. Cascaded H-Bridge Converters

The concept of cascaded H-bridge (CHB) converter was first introduced in [15]. After that in the late 1990s, the CHB converter was further studied and tested in [16]. The CHB converter consists of series connected H-bridge power cells. A typical H-bridge power cell is shown in Figure 1.10. The series-connected power cells naturally increase the voltage and power level of the CHB converters. The number of the power cell mainly depends on the operation voltage, the harmonic requirements, and the budget for the system [17]. What is more, for a CHB multilevel converter with k power cells, it will be able to generate $2k + 1$ level output voltages, which results in reduced harmonics in the output voltages and improved power quality [16]. The main drawback of the CHB converter is that it requires large number of dc sources for the H-bridge, which increases the cost.

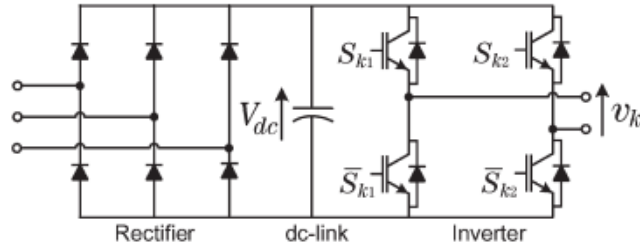


Figure 1.10 CHB power cell [17]

1.2.2 Rotor speed and position sensorless control

Implementation of the PMSG control algorithms such as field oriented control (FOC) and direct torque control (DTC) requires information on the rotor position and speed. Conventional methods to achieve the rotor position information are based on the encoders or transducers. However, the presence of the electrical sensors in the wind turbine PMSG reduces the reliability of the system due to the oscillation of the rotor shaft, as well as the harsh environment in which the WECSs are usually operated. Thus, research for sensorless control has become an attractive aspect.

Rotor position sensorless control algorithms can be sorted into two categories based on the operation speed of the PMSG, rotor saliency detection based low/zero speed sensorless control and back EMF based high speed PMSG rotor position sensorless control.

From the late 1990s, more and more investigations have been made on the topic of low/zero speed PMSG rotor position sensorless control. By detecting the rotor saliency (rotor saliency is caused due to the unevenly distributed reluctance in the rotor surface) of

the PMSG, the rotor position and speed information is achievable. In [18] and [19], the high frequency (HF) signal injection based sensorless control algorithm was introduced. This algorithm includes HF voltage injection and HF current injection. The basic principle of the former one is that by superimposing HF voltages into the stator of the PMSG, it will produce corresponding HF currents which will vary with the position of the rotor due to the saliency of the rotor. The sensed currents are then processed and demodulated to produce the information of the rotor position. Similarly, the basic principle of the HF current injection method is that by superimposing HF currents into the stator and detecting the HF voltages, the rotor position is achievable. The HF signal injection control approach has the advantages that it has good performance in low/zero speed application and it is robust to the variation of the parameters of the PMSG. However, this method requires the motor to have rotor saliency, thus is not applicable to surface-mounted PMSGs which has no rotor saliency.

As stated earlier, the back EMF based sensorless control algorithms are suitable for high speed PMSG applications. Several important back EMF based sensorless control algorithms are: (1) back EMF zero crossing detection control, (2) flux linkage estimator based sensorless control, and (3) sliding mode observer based sensorless control.

The back EMF zero crossing detection control was introduced in [20], this sensorless control algorithm is widely applied in the control of brushless DC (BLDC) machine. Its basic principle is that by detecting the back EMF zero crossing point of the phase winding which is not energized, the position information of the rotor is achievable [47]. Thus, the hall sensors in the BLDC machine can be eliminated. This method possesses the merits that it is easy to implement and does not need low pass filter.

However, it also has the drawback that the error of this method is considerable at low speed since the induced back EMF in the stator windings is small.

Flux linkage estimator based sensorless control was introduced in [21] in 1991. This method is usually used to estimate the rotor position and speed for surface-mounted permanent magnet synchronous machines (PMSMs) [22]. In the flux linkage estimator based sensorless control algorithm, the line-to-line voltages and currents are sensed, and thus the back EMF can be calculated based on the sensed voltages and currents, as well as the parameters of the PMSM. Hence, the stator flux linkage space vector can be calculated by integrating the back EMF. From the stator flux linkage space vector, the rotor position and speed can be easily calculated. This control algorithm is easy to implement, and does not need large computation efforts. However, the flux linkages estimated by the integral operation usually have integral errors due to the drift and offset in the integrators [23], and this error became considerable when the motor speed is low. A lot of investigations have been carried out to overcome this issue [24] [25] [26].

Sliding mode observer, which is one the most attractive rotor position self-sensing methods proposed in the literature, has been introduced to estimate ac machines' parameters and its robustness to the motor parameter variation has been verified [27]-[36]. Sliding mode control is a branch of the variable structure control, and its basic principle is that by building an observer based on the sensed stator voltages, stator currents, and the parameters of the PMSG, the estimated stator currents of the PMSG can be calculated and compared with the sensed stator currents, the error of the sensed and estimated currents will change the feedback structure of the control system, to make the observer operate on a predefined sliding surface. Thus, the sliding mode occurs. With the

estimated back EMF, the rotor position angle and speed can be easily calculated [37]. However, when the operation speed of the machine is low, the value of the back EMF will be small. Thus, the accuracy of the rotor position and speed estimation will be reduced. Another drawback of the sliding mode control is that the inherent chattering effect due to the variable structure feedback loop will bring noise to the system which results in an increase of the torque ripple of the PMSG [36].

1.3 Thesis Contribution and Organization

This thesis studies and reviews the control algorithms for the wind turbine permanent magnet synchronous generator systems in order to achieve a maximum power capture efficiency for the system. Furthermore, a sliding mode observer based rotor position and speed self-sensing control method is analyzed to eliminate the speed sensor mounted on the rotor shaft. The control algorithms are applied to a 2 MW wind turbine permanent magnet synchronous generator system and a simulation study is performed to validate the control methods.

The first chapter of the thesis introduces the background of the wind energy generation systems and the development of the wind power industry. Moreover, the literature review of the power electronics for wind turbine systems and several important sensorless control algorithms has been made.

Chapter 2 presents the mathematical modeling of the wind turbine model, as well as the PMSM model. As a matter of fact, a rigorous mathematical model of the wind turbine and the PMSM is the prerequisite for the design of the machine control

algorithms and the analysis of the steady-state characteristics of the wind energy conversion systems.

In Chapter 3, the control methods for the generator-side converter are analyzed. The optimal tip speed ratio based maximum power point tracking (MPPT) control algorithm was given. The FOC approach is introduced to control the speed of PMSG. The simulation results are presented to validate the proposed control methods.

In Chapter 4, the voltage oriented control (VOC) approach to regulate the active and reactive power injected into the grid is analyzed. With the application of the VOC approach, the unity power factor of the grid-side converter can be achieved and the quality of the power injected into the grid can be improved.

In Chapter 5, we propose a sliding mode observer (SMO) based rotor position and speed sensorless control algorithm to increase the reliability of the wind turbine PMSG systems, which were equipped with the rotor mounted speed sensors. The principle of the SMO based control is given and the simulation results are presented to validate the proposed algorithm.

Chapter 2: Modeling and Analysis of Direct-Drive Permanent Magnet Synchronous Generator Wind Turbine Systems

The main components of a direct-drive permanent magnet synchronous generator (PMSG) wind turbine are the wind turbine and the PMSG. The wind turbine captures the power from the wind for the system, and the PMSG transforms the mechanical power into electric power. In this chapter, the basic principles of the electric power generation will be introduced, and the mathematical models of the wind turbine and the PMSG will be developed and analyzed. These will further help in understanding the control algorithms for the system in the following chapters.

2.1 Modeling of Wind Turbines

In order to investigate the effectiveness of the energy conversion in wind energy conversion systems, first the available energy stored in the wind needs to be determined. Actually, the energy in the wind can be treated as the kinetic energy of a large amount of air particles with a total mass, m , moving at a wind velocity, V_W . Assuming that all the air particles are moving at the same speed and direction before impacting the rotor blades of the wind turbine, the potential available kinetic energy stored in the wind can be expressed according to the following expression:

$$E = \frac{1}{2} m V_W^2 \quad (2.1)$$

where, E , is the kinetic energy of the moving air particles, and m is the total mass of the air particles, while, V_W , is the velocity of the air particles (wind speed). Since the air

particles are moving at a speed, V_W , the total mass, m , of the particles for a period of time, t , can be rewritten as follows:

$$m = \rho A V_W t = \rho \pi r^2 V_W t \quad (2.2)$$

where, ρ , is the air density, and A is the swept area of the wind turbine rotor. Here, r , is the radius of the wind turbine rotor. Substituting expression (2.2) into (2.1), the kinetic energy of the air particles can be expressed as follows:

$$E = \frac{1}{2} \rho \pi r^2 V_W^3 t \quad (2.3)$$

From expression (2.3), the actual wind power at any instant of time can be represented as:

$$P_{Wind} = \frac{E}{t} = \frac{1}{2} \rho \pi r^2 V_W^3 \quad (2.4)$$

where, P_{Wind} , is the potentially available power in the wind. From expression (2.4), we can observe that the wind power is proportional to the cube of the wind speed, which means that a small increase of the wind speed will result in a large increase of the wind power. Moreover, the power can also be increased by enlarging the wind turbine rotor radius since the power is proportional to the square of this rotor radius. This is the reason that more and more large scale wind turbine systems (up to 10MW) are being investigated and contemplated nowadays.

However, the power expressed in expression (2.4) can only stand for the maximum potential power which is available when the wind with velocity, V_W , passes through the swept area of the wind turbine with radius, r . In fact, only a portion of this potentially available power can be captured by the wind turbine. In 1919, a German scientist Albert Betz had tried to express the action of the air particles (the wind) passing

through wind turbines [38]. According to Betz's idea, after impacting the rotor blades of the wind turbine, the velocity of the wind decreases from V_W to V_{W2} , which means that when the wind passes through the wind turbine blades, there is still some kinetic power left in the wind. The relationship between the power that is captured by the wind turbine and the potential maximum power in the wind can be expressed as follows:

$$C_p = \frac{P_{Turbine}}{P_{Wind}} \quad (2.5)$$

where, $P_{Turbine}$ is the mechanical power captured by the wind turbine, and C_p is the power coefficient of the wind turbine which can be expressed as follows [48]:

$$C_p = c_1(c_2 \frac{1}{\alpha} - c_3\beta - c_4\beta^x - c_5)e^{-c_6\frac{1}{\alpha}} \quad (2.6)$$

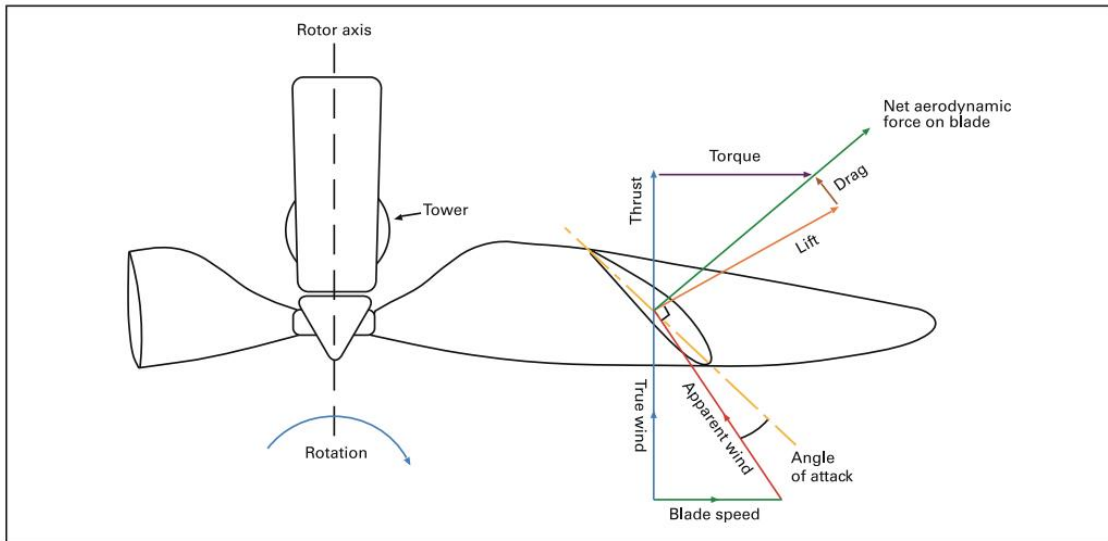
where,

$$\frac{1}{\alpha} = \frac{1}{\lambda + 0.08\beta} - \frac{0.035}{1 + \beta^3} \quad (2.7)$$

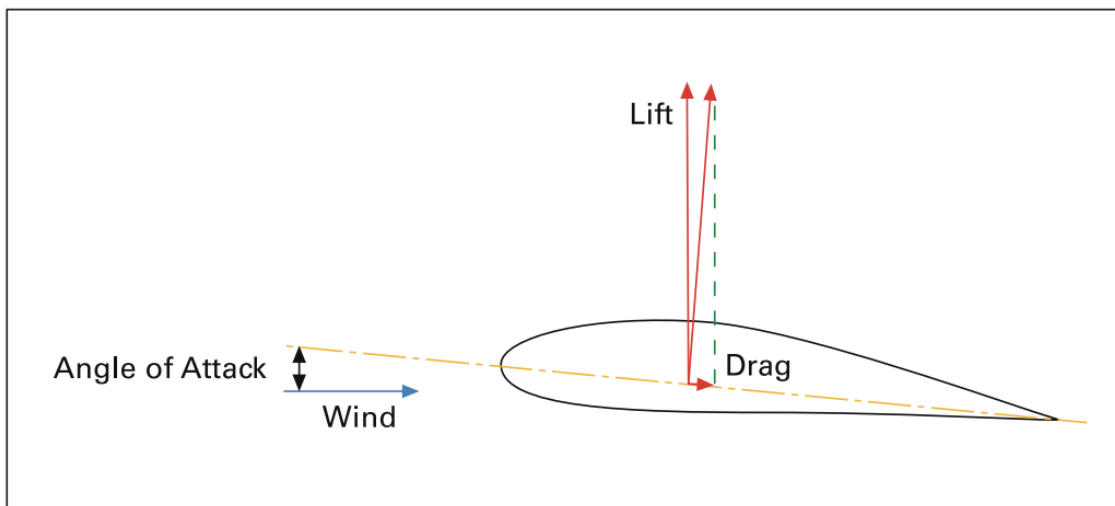
and,

$$\lambda = \omega_m r / V_w \quad (2.8)$$

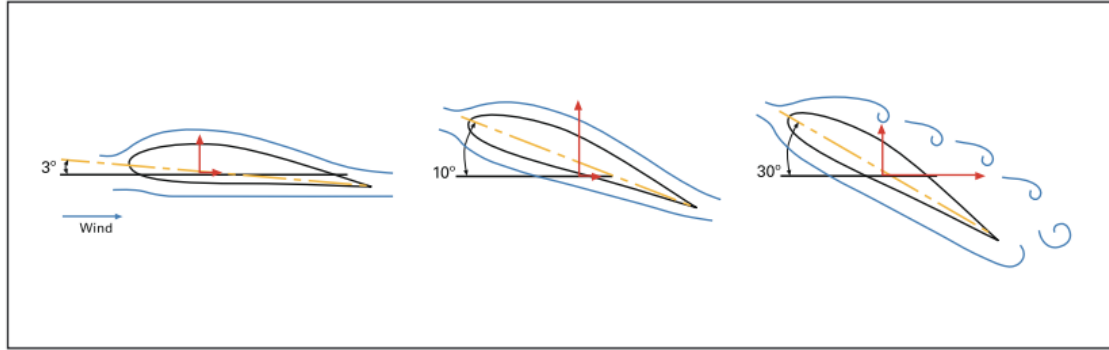
where, β , is the blade angle which is indicated in Figure 2.1, and λ is the tip speed ratio of the wind turbine, while, ω_m , is the angular speed of the wind turbine generator. The values of the coefficients ($c_1 \sim c_6$) depend on the type of the wind turbine.



(a). Blade angle schematic diagram



(b). Lift and drag force on the blade



(c). Blade at low medium and high angles of attack

Figure 2.1 Diagram of blade angle of wind turbine [39]

As can be seen in Figure 2.1, the blade angle indicates how does the wind velocity impact the wind turbine blades. The blade angle is the angle between the orientation of the blade and the wind velocity vector. When, $\beta = 0$, the blade is fully impacted by the wind velocity, and the wind turbine will capture the maximum power in the wind. The blade angle is usually controlled at zero degree when the wind speed is lower than the rated wind speed of the system to ensure a high efficiency of energy capture. When the wind speed becomes greater than the rated value, the power captured by the system will exceed the rated power if the blade angle stays unchanged at zero degree. It will make the generator and the power devices work under higher than rated output, which is harmful to the system if sustained for any length of time. Based on this concern, a control system for the modification of the blade angle according to different wind conditions is needed for the wind turbine. Accordingly, the power captured by the wind turbine can be rewritten as:

$$P_{Turbine} = \frac{1}{2} \rho \pi r^2 C_p(\lambda, \beta) V_w^3 \quad (2.9)$$

2.2 Modeling of Permanent Magnet Synchronous Machines

Permanent magnet synchronous machines/generators (PMSMs/PMSGs) play key role in direct-drive wind power generation systems for transforming the mechanical power into electrical power. A rigorous mathematical modeling of the PMSG is the prerequisite for the design of the machine control algorithms as well as the analysis of the steady-state and dynamic characteristics of wind energy conversion systems. In this section, the mathematical model of a PMSG in both the natural abc three-phase stationary reference frame and dq synchronously rotating reference frame will be developed, and the power and torque analysis of PMSGs will be given as well.

2.2.1 Modeling of a PMSM in the natural abc three-phase stationary reference frame

Before developing the mathematical model of the PMSM, several important assumptions need to be made: (1) the damping effect in the magnets and in the rotor are negligible; (2) the magnetic saturation effects are neglected; (3) the eddy current and hysteresis losses are neglected; (4) the back electromotive force (EMF) induced in the stator windings are sinusoidal; (5) for simplicity, all the equations of PMSMs are expressed in motor (consumer/load) notation, that is, negative current will be prevailing when the model refers to a generator. Negative current means that at the positive polarity of the terminal of a device the current is out of that terminal.

Figure 2.2 shows the cross-sectional view of a three-phase, two-pole PMSM. The fixed abc axes denote the direction of the MMFs (f_a , f_b and f_c) of the a , b and c phase windings, which are induced by the time varying three-phase AC currents in these stator phase windings. The flux caused by the permanent magnet is in the direction of the d -axis fixed at the rotor. Here, the dq -axes are rotating at the same angular speed of the PMs and rotor. Also, θ_r , denotes the angle between the d -axis and the stationary a -axis.

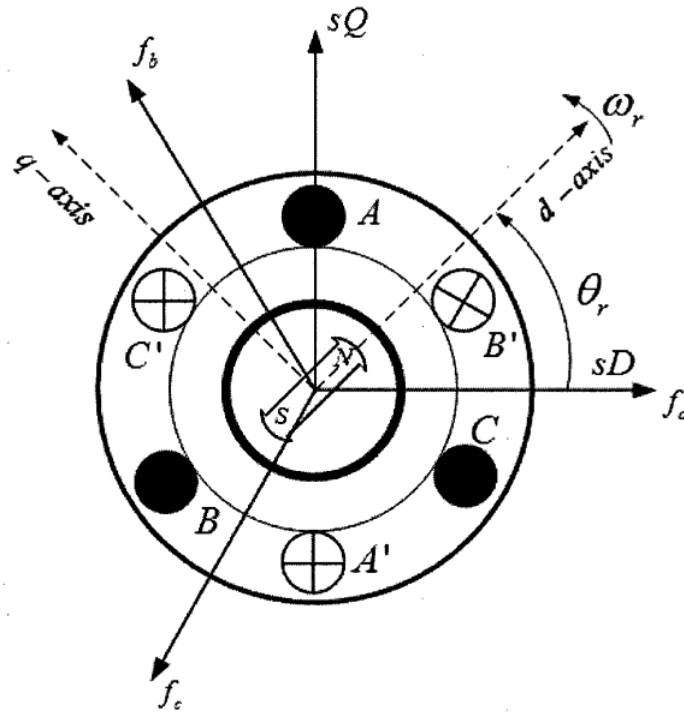


Figure 2.2 Cross-section view of the PMSM [40]

The state space relationship of the terminal voltages of the PMSM to the phase currents and the phase flux linkages due to the PMs and stator currents can be written as follows [41]:

$$\begin{bmatrix} v_{as} \\ v_{bs} \\ v_{cs} \end{bmatrix} = \begin{bmatrix} R_s & 0 & 0 \\ 0 & R_s & 0 \\ 0 & 0 & R_s \end{bmatrix} \cdot \begin{bmatrix} i_{as} \\ i_{bs} \\ i_{cs} \end{bmatrix} + \frac{d}{dt} \begin{bmatrix} \lambda_{as} \\ \lambda_{bs} \\ \lambda_{cs} \end{bmatrix} \quad (2.10)$$

Where, v_{as} , v_{bs} , and v_{cs} are the instantaneous a , b , and c three-phase stator voltages, and i_{as} , i_{bs} , and i_{cs} are the instantaneous three-phase stator currents. Here, R_s is the stator winding resistance per phase, and again, λ_{as} , λ_{bs} , and λ_{cs} are the instantaneous flux linkages induced by the three-phase AC currents and the PMs, which can be expressed in expanded form as follows [41]:

$$\begin{bmatrix} \lambda_{as} \\ \lambda_{bs} \\ \lambda_{cs} \end{bmatrix} = \begin{bmatrix} L_{aa} & L_{ab} & L_{ac} \\ L_{ba} & L_{bb} & L_{bc} \\ L_{ca} & L_{cb} & L_{cc} \end{bmatrix} \cdot \begin{bmatrix} i_{as} \\ i_{bs} \\ i_{cs} \end{bmatrix} + \begin{bmatrix} \lambda_r \cos(\theta_r) \\ \lambda_r \cos(\theta_r - \frac{2\pi}{3}) \\ \lambda_r \cos(\theta_r + \frac{2\pi}{3}) \end{bmatrix} \quad (2.11)$$

where, L_{aa} , L_{bb} , and L_{cc} , are the self-inductances of the a , b , and c three-phases, and L_{ab} , L_{ac} , L_{ba} , L_{bc} , L_{ca} , and L_{cb} are the mutual inductances between these phases, while, λ_r , is the rotor flux linkage caused by the permanent magnet. The self-inductances and mutual inductances are all functions of θ_r . Thus, all of the inductances are time varying parameters.

2.2.2 Modeling of the PMSM in the dq-axes synchronously rotating reference frame

The $dq0$ Park's transformation is a mathematical transformation which aims to simplify the analysis of synchronous machinery models, and was first introduced by R. H. Park in 1929 [42]. In the three-phase systems like PMSMs, the phase quantities which include stator voltages, stator currents, and flux linkages, are time varying quantities. By applying Park's transformation, which is in essence the projection of the phase quantities

onto a rotating two axes reference frame, the AC quantities are transformed to DC quantities which are independent of time. The abc to $dq0$ transformation can be expressed in matrix form as follows:

$$\begin{bmatrix} u_d \\ u_q \\ u_0 \end{bmatrix} = \sqrt{\frac{2}{3}} \begin{bmatrix} \cos(\theta_r) & \cos(\theta_r - \frac{2\pi}{3}) & \cos(\theta_r + \frac{2\pi}{3}) \\ -\sin(\theta_r) & -\sin(\theta_r - \frac{2\pi}{3}) & -\sin(\theta_r + \frac{2\pi}{3}) \\ \frac{\sqrt{2}}{2} & \frac{\sqrt{2}}{2} & \frac{\sqrt{2}}{2} \end{bmatrix} \begin{bmatrix} u_a \\ u_b \\ u_c \end{bmatrix} \quad (2.12)$$

The inverse Park's transformation is:

$$\begin{bmatrix} u_a \\ u_b \\ u_c \end{bmatrix} = \sqrt{\frac{2}{3}} \begin{bmatrix} \cos(\theta_r) & -\sin(\theta_r) & \frac{\sqrt{2}}{2} \\ \cos(\theta_r - \frac{2\pi}{3}) & -\sin(\theta_r - \frac{2\pi}{3}) & \frac{\sqrt{2}}{2} \\ \cos(\theta_r + \frac{2\pi}{3}) & -\sin(\theta_r + \frac{2\pi}{3}) & \frac{\sqrt{2}}{2} \end{bmatrix} \begin{bmatrix} u_d \\ u_q \\ u_0 \end{bmatrix} \quad (2.13)$$

In expressions (2.12) and (2.13), u_{abc} and u_{dq0} can represent the stator voltages, stator currents or flux linkages of the AC machines, respectively. Considering that under balanced conditions, $u_0=0$, the voltage function of the PMSM in the dq -axes reference frame can be expressed as follows [41]:

$$v_{ds} = R_s i_{ds} + L_d \frac{di_{ds}}{dt} - \omega_e L_q i_{qs} \quad (2.14)$$

$$v_{qs} = R_s i_{qs} + L_q \frac{di_{qs}}{dt} + \omega_e L_d i_{ds} + \omega_e \lambda_r \quad (2.15)$$

Where, v_{ds} and v_{qs} , are the instantaneous stator voltages in the dq -axes reference frame, and i_{ds} and i_{qs} , are the instantaneous stator currents in the dq -axes reference frame. Here, L_d and L_q , are the d -axis and q -axis inductances, and ω_e is the electrical angular speed of

the rotor, while, λ_r , is the peak/maximum phase flux linkage due to the rotor-mounted PMs. According to expressions (2.14) and (2.15), the equivalent circuits of the PMSM in the dq -axes reference frame can be drawn as shown in Figure 2.3:

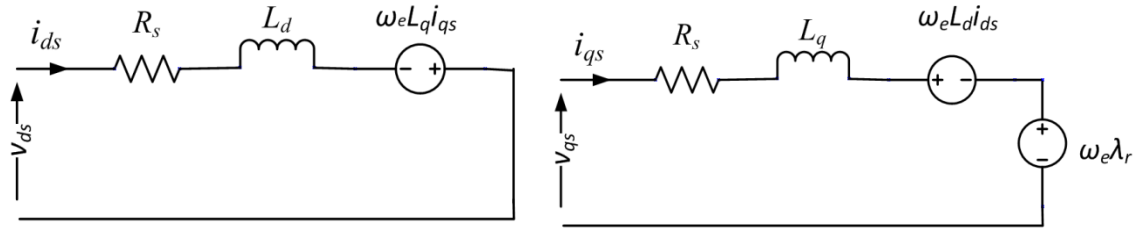


Figure 2.3 The dq -axes equivalent circuits of a PMSM

2.2.3 Power and torque analysis of a PMSM

For any PMSM, the electrical power input can be expressed in the abc reference frame as follows:

$$P_{abc} = v_{as}i_{as} + v_{bs}i_{bs} + v_{cs}i_{cs} \quad (2.16)$$

or in the dq -axes reference frame as follows:

$$P_{dq} = \frac{3}{2}(v_{ds}i_{ds} + v_{qs}i_{qs}) \quad (2.17)$$

As a part of the input power, in the motoring mode, the active power is the power that is transformed to mechanical power by the machine, which can be expressed as follows:

$$P_{em} = \frac{3}{2}(e_d i_{ds} + e_q i_{qs}) \quad (2.18)$$

where,

$$e_d = -\omega_e L_q i_{qs} = -\omega_e \lambda_q \quad (2.19)$$

and
$$e_q = \omega_e L_d i_{ds} + \omega_e \lambda_r = \omega_e \lambda_d \quad (2.20)$$

Here, e_d and e_q , are the back EMFs in the dq -axes reference frame, and λ_d and λ_q are the dq -axes flux linkages. Substituting expressions (2.19) and (2.20) into (2.18), the active power can be re-expressed as follows:

$$P_{em} = \frac{3}{2} \omega_e (\lambda_d i_{qs} - \lambda_q i_{ds}) \quad (2.21)$$

Hence, the electromagnetic torque developed by a PMSM can be deduced as follows:

$$T_e = \frac{P_{em}}{\omega_e / \frac{p}{2}} = \frac{3}{2} \left(\frac{p}{2} \right) (\lambda_d i_{qs} - \lambda_q i_{ds}) \quad (2.22)$$

or
$$T_e = \frac{3}{2} \left(\frac{p}{2} \right) (\lambda_r i_{qs} + (L_d - L_q) i_{qs} i_{ds}) \quad (2.23)$$

where, p is the number of poles in the machine.

Chapter 3: Control of Generator-Side Converter

In wind turbine PMSG systems, three system variables need to be strictly controlled [6]: (1) the optimal power generated by the PMSG at different wind speed levels; (2) the active and reactive power injected into the grid; (3) the DC bus voltage of the back to back converter. Figure 3.1 shows a direct-drive wind turbine PMSG fed by a back-to-back converter. In this system, the generator-side converter regulates the speed of the PMSG to implement the MPPT control. Meanwhile, the grid-connected converter controls the active and reactive power injected into the grid.

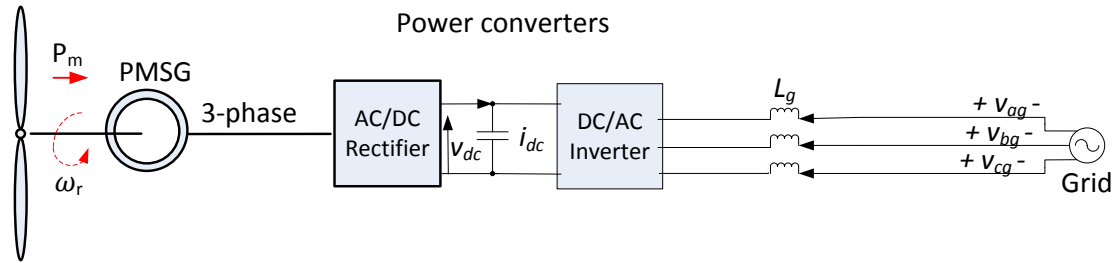


Figure 3.1 Direct-drive PMSG system

This chapter will focus on analyzing the control methods for the generator-side converter. The optimal tip speed ratio based maximum power point tracking (MPPT) control is analyzed in this chapter. Two important PMSG control algorithms, the direct torque control (DTC) and the field oriented control (FOC), are analyzed and compared. Then, the simulation results of the generator-side converter control are given to validate the principles of control algorithms.

3.1 Maximum Power Point Tracking Control

Direct-drive PMSGs have the capability to work in a wide speed range. According to the intensity of the wind, the wind turbine generators need to be controlled to operate in three different modes as shown in Figure 3.2 [6]:

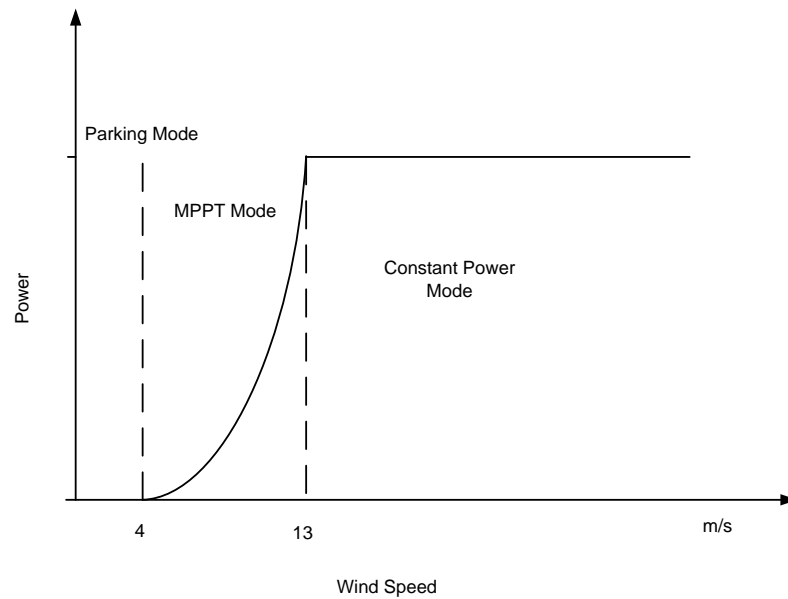


Figure 3.2 Wind turbine power-speed characteristic for the specific wind turbine analyzed in this thesis

1. Parking Mode: when the wind speed is lower than the cut-in speed which is 4 m/sec (9mph) in this system, the wind turbine will not rotate but stay in parking status due to the fact that the electrical power generated by the PMSG system is insufficient to compensate for the internal power losses in this system. Therefore, the wind turbine is kept in parking mode by a mechanical brake;

2. MPPT mode: when the wind speed is greater than the cut-in speed, the wind turbine system starts to work and generate electrical power. Because the wind speed is in a relatively low range in the MPPT mode, the power captured by the wind turbine is below its rated value, the MPPT control needs to be applied to ensure a maximum efficiency of power capture. The MPPT mode ends when the wind speed is greater than the rated wind speed, $13m/sec$ (29mph), for this case-study system.

3. Constant power region: when the wind speed becomes greater than the rated value, the power generated by the system will be larger than its rated power if the MPPT control is still applied. This will increase the electrical stress on the PMSG and the power processing devices, and would further damage them. Therefore, the blade angle of the wind turbine blades needs to be properly controlled in the strong wind range to keep the system operating within its rated output condition. As its name implies, this is constant power region.

In Chapter 2, the expression of the mechanical power captured by the wind turbine has been expressed as:

$$P_{Turbine} = \frac{1}{2} \rho \pi r^2 C_p(\lambda, \beta) V_w^3 \quad (2.7)$$

the power coefficient, $C_p(\lambda, \beta)$, can be expressed in Figure 3.3.

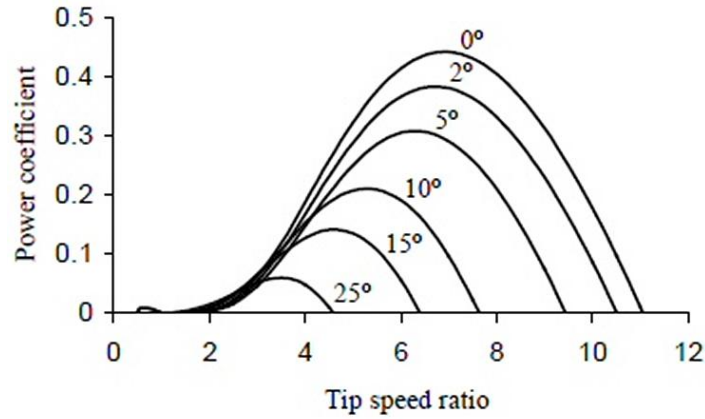


Figure 3.3 Power coefficient characteristics

As shown in equation (2.7), to control the captured mechanical power, $P_{Turbine}$, at given wind speed, V_W , the only controllable term is the power coefficient, $C_p(\lambda, \beta)$. The power coefficient characteristic is shown in Figure 3.3. As can be seen in this figure, different power coefficient curves correspond to different blade angles. For each case, there is an optimal tip speed ratio, λ , which contributes to a peak power coefficient value which, in turn, leads to a maximum power capture, $P_{Turbine}$. In the MPPT operation mode, the pitch angle is usually kept at zero degree. In order to achieve the peak power coefficient value in the zero degree pitch angle curve in Figure 3.3, the tip speed ratio needs to be controlled at the optimal value. From expression (2.8), the control of the tip speed ratio is actually the control of the rotor speed of the PMSG. A simplified scheme of tip speed ratio control is shown in Figure 3.4. From this figure, the wind speed information is sensed by a sensor and sent to a microcontroller, from which the reference speed of the PMSG can be calculated according to the optimal tip speed ratio.

Consequently, the generator speed will reach its reference value in the static state, and then the MPPT control is achieved.

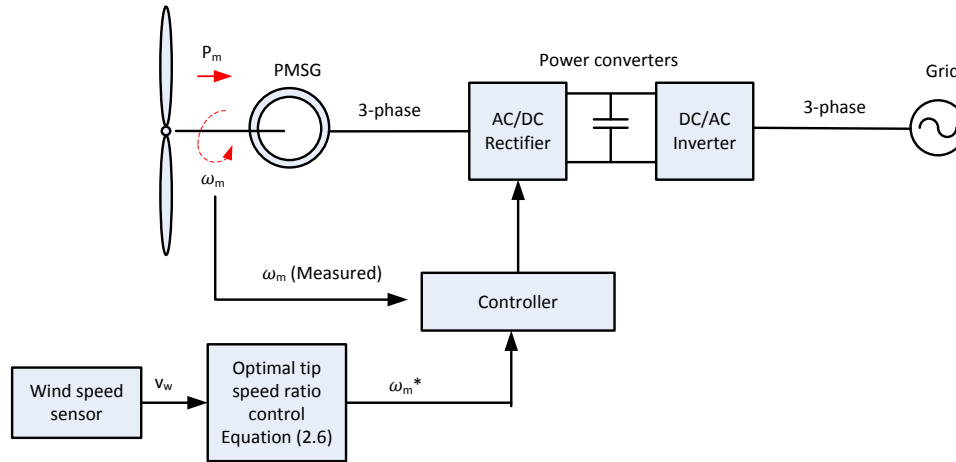


Figure 3.4 Tip speed ratio control scheme

3.2 Comparison between Direct Torque Control and Field Oriented Control

Direct torque control (DTC) and field oriented control (FOC) are two of the most commonly applied algorithms for the control of PMSMs. The DTC approach was first developed and presented by I. Takahashi from Japan [43]. The basic principle of the DTC approach is that the stator flux linkage and the electromagnetic torque are estimated and compared with their reference values. Based on the control algorithm of mitigating the errors between the reference and estimated values, the reference torque and flux can be achieved by controlling the inverter states. The FOC approach was pioneered by F. Blaschke in 1970s [44]. The FOC approach has been and continues to be a significant factor in PMSMs control, which makes it possible that PMSMs can be controlled as

easily as DC machines. In the FOC approach, the dq -axes are rotating at the rotor electrical angular speed with the d -axis aligned with the rotor flux direction. Thus, the flux producing current component, i_{ds} , and the torque producing current component, i_{qs} , are along the d -axis and q -axis, respectively. Thus, the dq -axes currents can be controlled independently by two closed loop controls in the FOC approach, which indirectly controls the speed and the torque of the PMSMs.

When choosing one control strategy of either DTC or FOC for the generator-side converter control, their merits and drawbacks need to be analyzed and compared according to the operation requirements of the direct-drive PMSG systems. The DTC approach has the advantages that the electromagnetic torque can be changed very fast by changing the reference, and no coordinate transforms and PI controllers are needed which decreases the computational effort. On the other hand, the DTC approach also presents some disadvantages such as: (1) the difficulty to control the torque at very low speed; (2) the high current and torque ripples; and (3) the high noise level at low speed. When it comes to the FOC approach, although its implementation requires large computational effort including PI control and coordinate transformations, it possesses the following merits: (1) fast speed and torque response; (2) outstanding low speed performance; and (3) low current and torque ripples. For the application of direct-drive PMSG systems, the PMSGs are directly driven by the wind turbine without a gearbox, which means that their operation speeds are always in a relatively low range. Moreover, the torque ripples of the direct-drive PMSGs should be controlled at a low level to decrease the mechanical stresses on the wind turbine. On the basis of the analysis above, the FOC approach was found to be more suitable for the direct-drive PMSG systems than the DTC approach.

3.3 Field Oriented Control based Generator-Side Converter Control

In Chapter 2, the torque expression of the PMSMs has been developed as follows:

$$T_e = \frac{3}{2} \left(\frac{p}{2} \right) (\lambda_r i_{qs} + (L_d - L_q) i_{qs} i_{ds}) \quad (2.27)$$

For a surface mounted PM machine (SPM) which is applied in the case study system in this thesis, the d -axis and q -axis inductances are equal ($L_d = L_q$). Thus, the torque expression can be simplified and rewritten as follows:

$$T_e = \frac{3}{2} \left(\frac{p}{2} \right) \lambda_r i_{qs} \quad (3.1)$$

In order to achieve the maximum torque per ampere, the d -axis current is set at zero ($i_{ds} = 0$). In expression (3.1), λ_r is the flux linkage due to the permanent magnets which is a constant. Thus, there will be a linear relationship between the electromagnetic torque and the q -axis current, i_{qs} , such that the electromagnetic torque can be easily controlled by regulating the q -axis current. The phasor diagram for the FOC approach is shown in Figure 3.5, and the control scheme of the generator-side converter is shown in Figure 3.6.

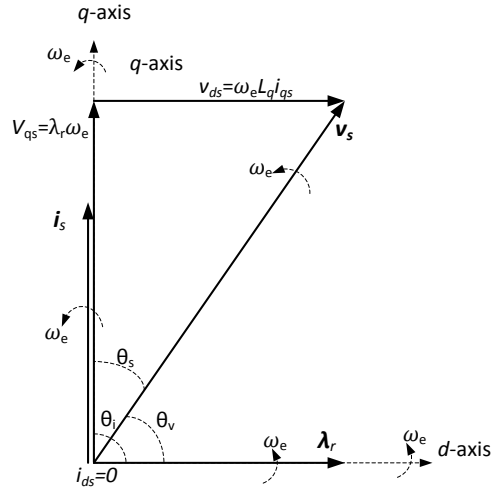


Figure 3.5 Phasor diagram of the FOC

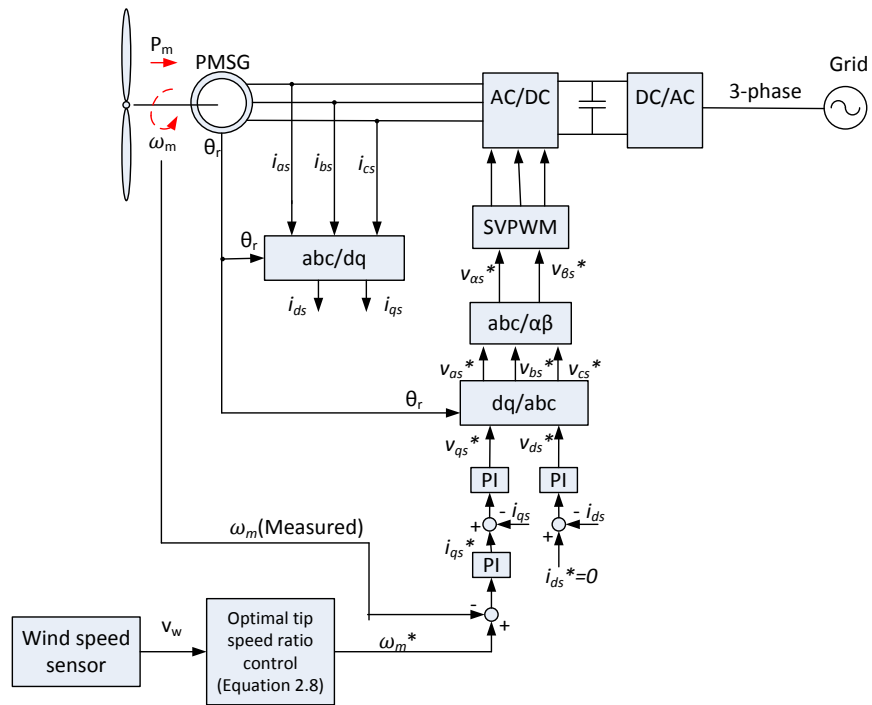


Figure 3.6 Generator-side control scheme

As stated earlier, the FOC approach coupled to the optimal tip speed ratio based MPPT control strategy is applied here as the control algorithm for the generator-side power converter. In Figure 3.6, there are three feedback loops in the control system which are: (1) the speed control loop, (2) the d -axis current control loop, and (3) the q -axis current control loop. In the speed loop, at every sampling time, the actual speed of the generator sensed by an encoder mounted on the shaft of the rotor is compared to its reference value, which in turn is generated by the optimal tip speed ratio control, and then the error is sent to a PI controller which will output the reference q -axis current, i_{qs}^* . Meanwhile, the reference d -axis current, i_{ds}^* , is always set at zero. To acquire the feedback current signals, three-phase stator currents are sensed and transformed into the dq -axes reference frame according to Park's transformation. The reference stator voltages are then being achieved by PI controllers in the dq -axes current control loops. Here, the space vector pulse width modulation (SVPWM) approach is applied as the modulation strategy in this system, because it generates less harmonic distortion in the output stator voltages/currents and provides more efficient use of the DC supply voltages than the conventional sinusoidal pulse width modulation (SPWM). The principle of the SVPWM will be elaborated in next chapter. The outputs of the SVPWM model are six PWM signals to control the ON/OFF state of the six IGBT switches in the generator-side converter.

3.4 Simulation Results and Analysis

Simulation studies were carried out in MATLAB-Simulink to validate the chosen case-study system. In order to approximate the performance of the discrete-time

microcontrollers which are commonly used in industrial control systems, such as the digital signal processors (DSPs), the chosen simulation type in Simulink is set as a discrete-type with a sample time of 2 microsecond. The parameters of the case-study wind turbine and the associated PMSM are shown in Table 3.1. Figure 3.7 shows the circuit diagram of the system built in Simulink, and Figure 3.8 shows the control scheme of the FOC approach in Simulink.

Table 3.1 Parameters and operating conditions of the generator side control system [6]

Generator Type	PMSG, 2.0 MW, 690 V, 9.75 Hz, non-salient pole
Rated Mechanical Power	2.0 MW
Rated Apparent Power	2.2419 MVA
Rated Power Factor	0.8921
Rated Rotor Speed	22.5 r/min
Number of Pole Pairs	26
Rated Mechanical Torque	848826 Nm
Rated Rotor Flux Linkage	5.8264 (rms)
Stator Winding Resistance	0.821 m Ω
<i>d</i> axis Synchronous Inductance	1.5731 mH
<i>q</i> axis Synchronous Inductance	1.5731 mH
Wind Turbine Rotor Radius	34 m
Wind Turbine Optimal Tip Speed Ratio	6.16
IGBT Modulation Frequency	1.5 kHz

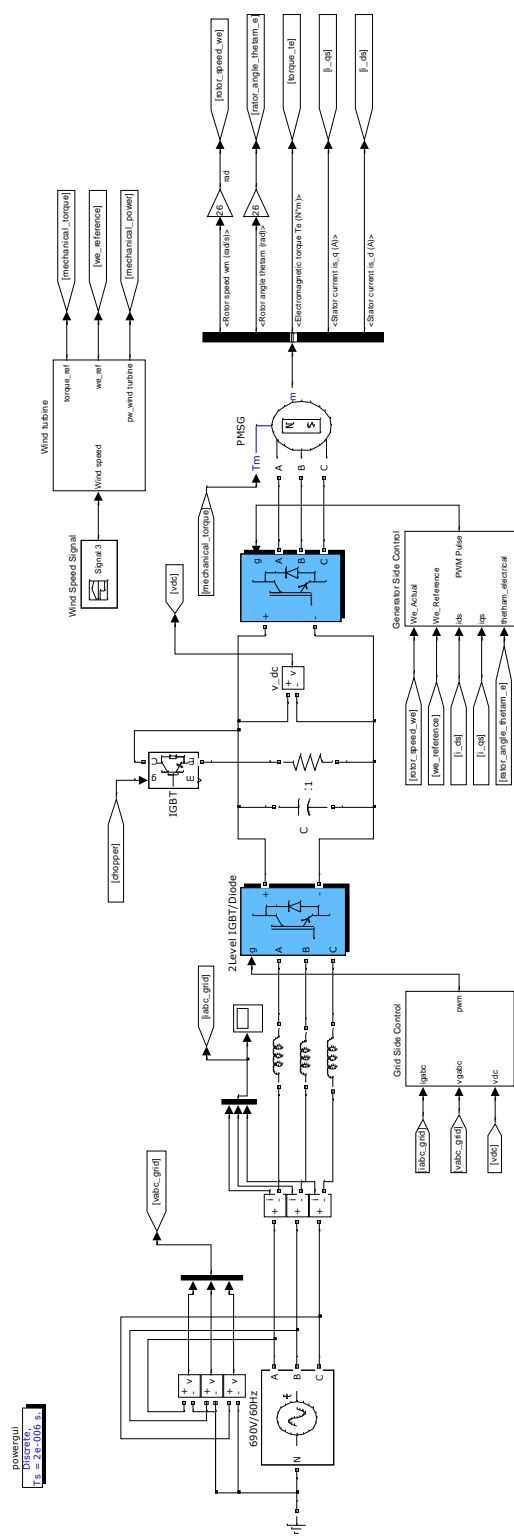


Figure 3.7 Control diagram of the system

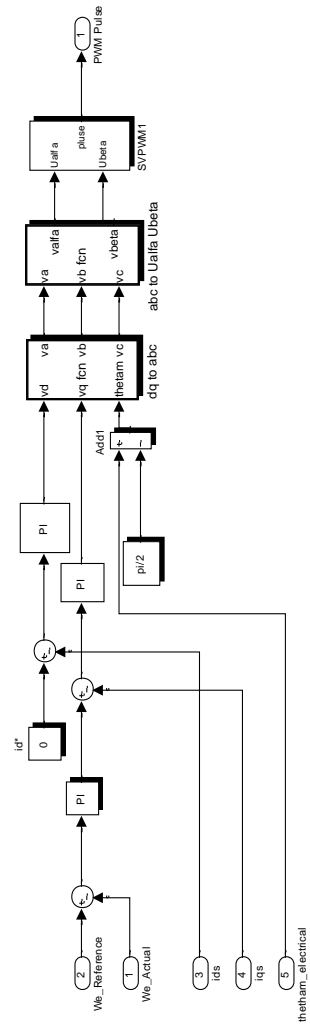


Figure 3.8 Control diagram of the FOC

Simulation results of the proposed system are shown in Figures 3.9 through 3.17. Figure 3.9 shows the wind speed input for the system. As can be seen in this figure, from 0-1.3s, the wind speed increases from 4m/s (cut-in speed) to 8m/s and then is maintained constant at 8m/s till 1.3s. In this wind speed range, we can investigate the performance of the proposed MPPT control strategy. From 1.3-2.6s, the wind speed increases from 8m/s to 13m/s (rated wind speed). In this wind speed range, the performance of the system in its rated condition can be evaluated. After that, the wind speed continues to increase to 15m/s which exceeds its rated wind speed. Thus, the constant power control algorithm to deal with the high wind speed can be investigated. Shown in Figure 3.10 is the actual rotor speed in electrical radians per second. Figure 3.11 shows the corresponding three-phase stator currents. The d -axis and q -axis currents are shown in Figure 3.12 and Figure 3.13, respectively. Meanwhile, Figure 3.14 shows the electromagnetic torque developed by the generator. The electrical power developed by the generator is shown in Figure 3.15.

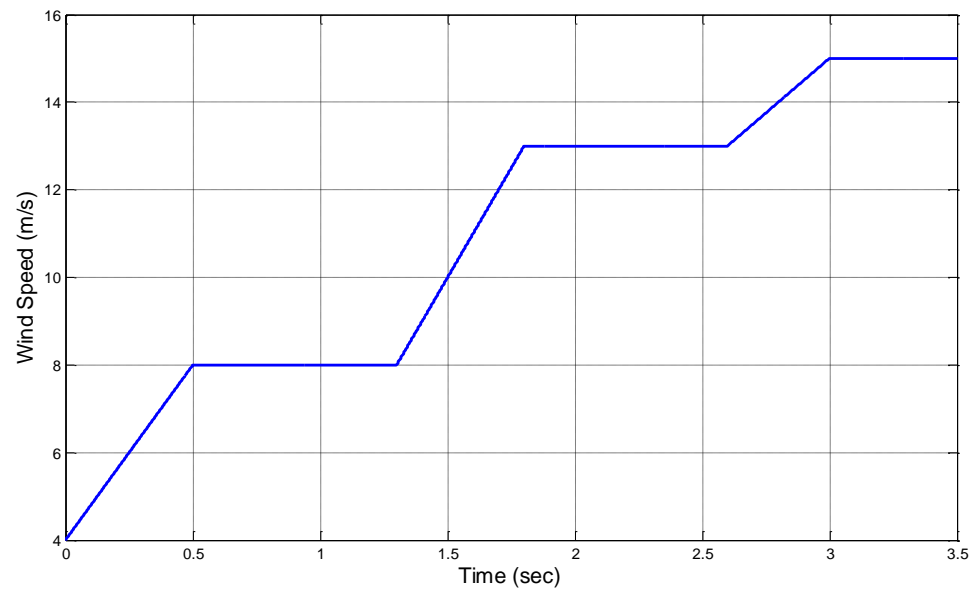


Figure 3.9 Wind speed input for the wind power generation system

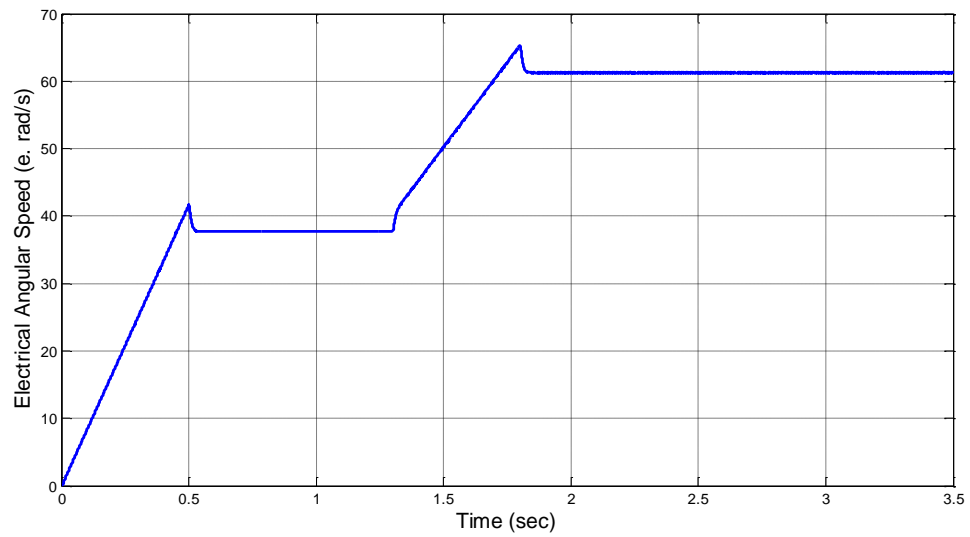


Figure 3.10 Actual electrical angular speed of the PMSG

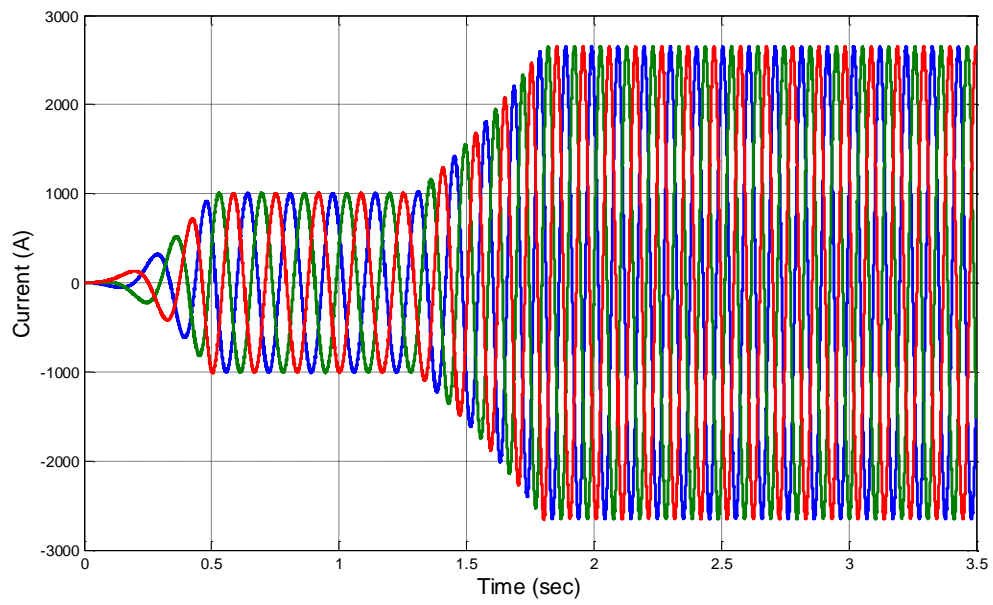


Figure 3.11 Three-phase stator currents of the PMSG

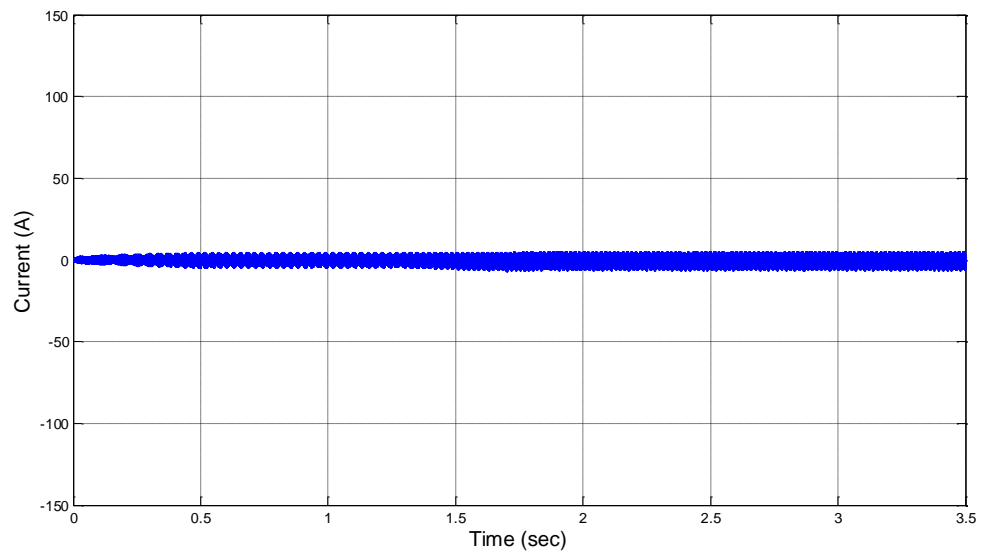


Figure 3.12 d -axis current of the PMSG

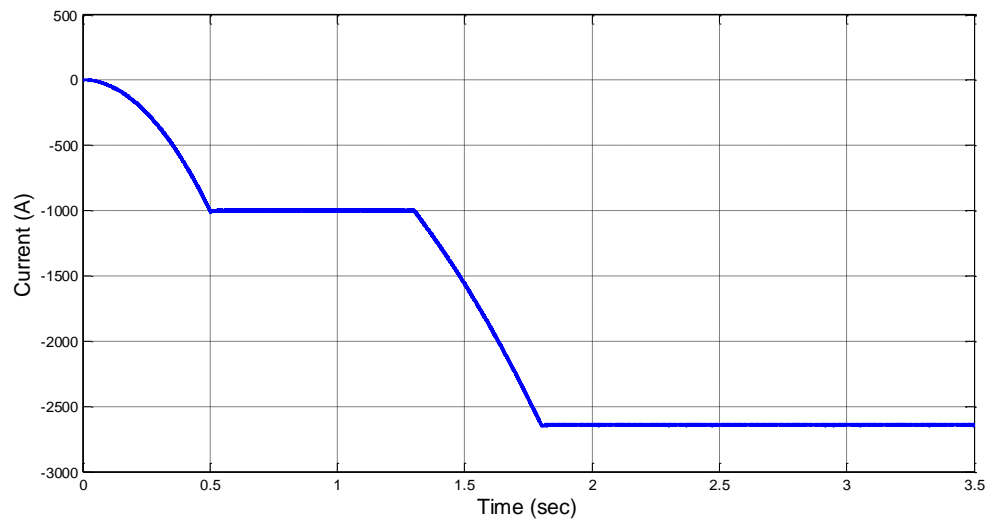


Figure 3.13 q -axis current of the PMSG

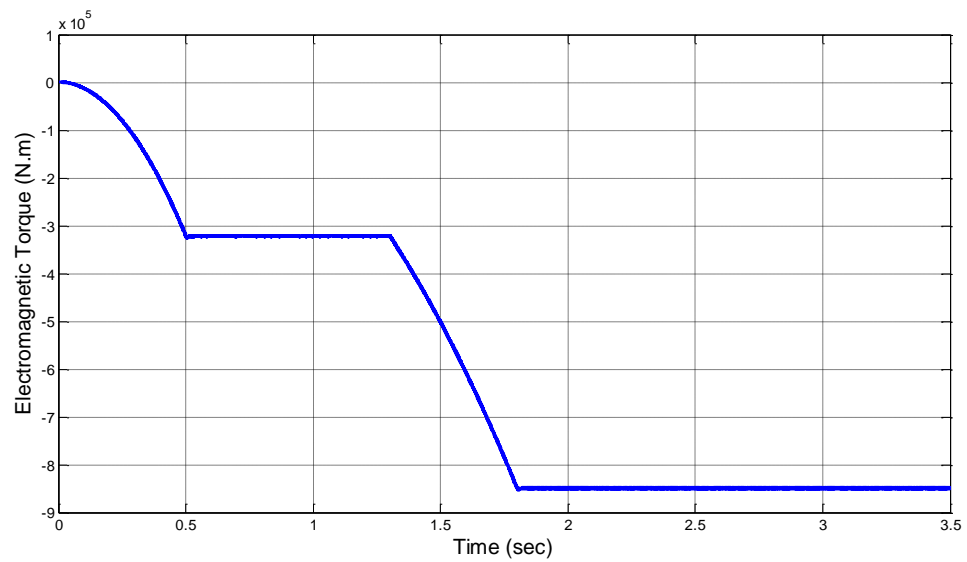


Figure 3.14 Electromagnetic torque developed by the PMSG

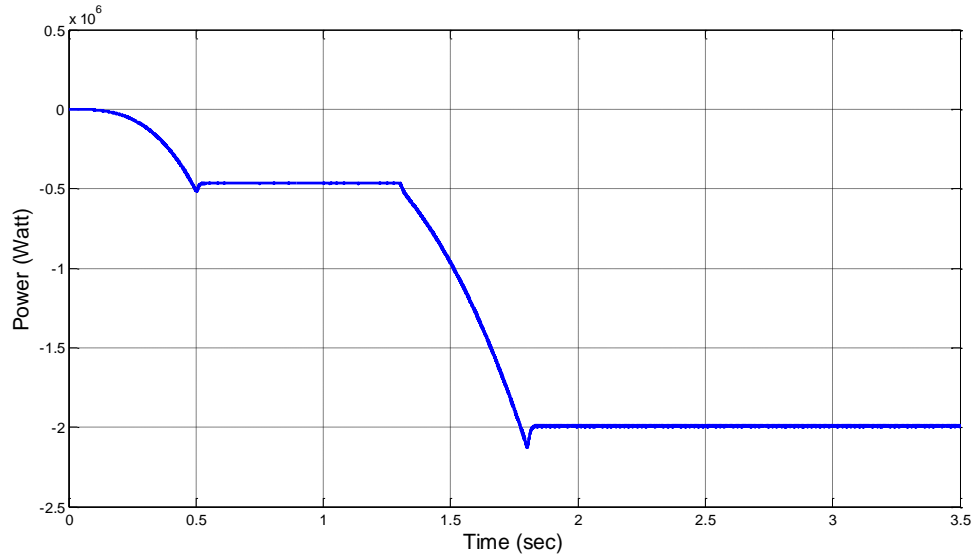


Figure 3.15 Electrical power generated by the PMSG

As can be seen in the simulation results, according to different wind speed levels, the system performance has different characteristics best described as follows:

(1) From 0-1.3s: the wind speed starts to increase from the cut-in speed ($4m/s$), which means that the generated electrical power is sufficient to compensate for the internal power consumption losses. Thus, the wind turbine begins to rotate and the PMSG begins to generate electrical power. As shown in Figures 3.10 through 3.15, with the increase of the wind speed, the stator currents, electromagnetic torque, and the generated electrical power are gradually increased. As can be seen in Figure 3.12, the d -axis current is controlled to be zero, which contributes to a linear relationship between the q -axis current and the electromagnetic torque. From 0.5s, the wind speed reaches $8m/s$ and stops increasing, soon after that the system comes to the steady state. In the steady state, the theoretical values of the generator speed, q -axis current, electromagnetic torque, and generated electrical power can be calculated to verify the simulation results.

According to expression (2.8), when the wind speed is $8m/s$, the reference generator speed in electrical radians is:

$$\omega_e = \left(\frac{p}{2}\right) \frac{\lambda V_w}{r} = 26 \cdot \frac{6.16 \cdot 8}{34} = 37.7 \text{ (e.rad/s)}$$

The mechanical power captured by the wind turbine based on expression (2.9) is:

$$P_{Turbine} = \frac{1}{2} \rho \pi r^2 C_p(\lambda, \beta) V_w^3 = 0.5 \cdot 1.225 \cdot \pi \cdot 34^2 \cdot 0.41 \cdot 8^3 = 0.466 \cdot 10^6 \text{ W}$$

The mechanical torque on the rotor shaft can be calculated as:

$$T_m = \frac{P_{Turbine}}{\omega_m} = \frac{0.466 \cdot 10^6}{37.7/26} = 322258.2 \text{ (Nm)}$$

It should be noticed that the torque should be denoted as a negative value because the PMSM is working in the generator mode. When the system reaches the steady state, the mechanical torque is equal to the electromagnetic torque. According to expression (3.1), the q -axis current can be calculated as follows:

$$T_e = T_m = \left(\frac{3}{2}\right) \left(\frac{p}{2}\right) \lambda_r i_{qs}$$

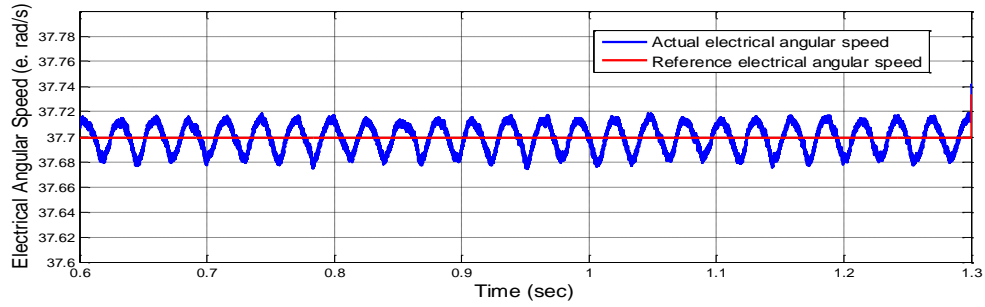
$$i_{qs} = \frac{T_m}{\left(\frac{3}{2}\right) \left(\frac{p}{2}\right) \lambda_r} = \frac{-322258.2}{1.5 \cdot 26 \cdot 8.2398} = -1002.8 \text{ (A)}$$

Showing in Figure 3.16 are the simulation results of the generator speed ($e.rad/s$), q -axis current, electromagnetic torque, and the generated electrical power versus their calculated values when the system is in the steady state and the wind speed is $8m/s$. As shown in these figures, the actual values of these performance variables correspond well

to their calculated values, except that the generated electrical power is slightly smaller than the mechanical power input into the system. This is due to the internal power losses in the system. Based on the analysis above, the control objectives for the low wind speed range were achieved and the optimal power is captured and transformed by the PMSG.

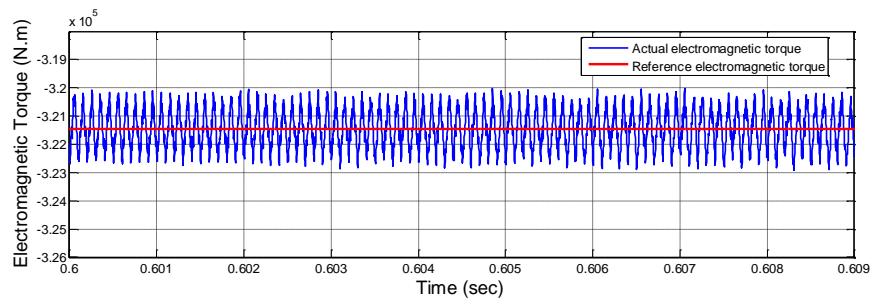
(2) From 1.3-2.6s: starting from 1.3s, the wind speed increases from 8m/s to 13m/s , which is the rated wind speed of the system. As shown in Figures 3.10 through 3.15, with the increase of the wind speed, stator currents, electromagnetic torque, and generated electrical power gradually increase to their rated values which are shown in Table 3.1. The comparison between the actual values and the rated values of the system parameters are shown in Figure 3.17. From these figures, the simulation results correspond well to the rated values. Again, the reason that the actual electrical power generated by the PMSG is slightly lower than the mechanical power input is due to the internal power losses. Thus, conclusions can be made that the control objective was achieved under the rated condition of the system.

(3) From 2.6-3.5s: the wind speed keeps increasing and exceeds the rated value. In order to limit the power input to prevent the electrical and mechanical stress on the system, the constant power control was applied in this wind speed range. That is, the mechanical power input of the system is kept at 2MW and the generator speed is controlled at its rated value instead of increasing with the wind speed. As can be seen in Figures 3.10 through 3.15, during time 2.6-3.5s, all of the system performance variables including the stator current, electromagnetic torque, and generated electrical power are kept at their rated values.

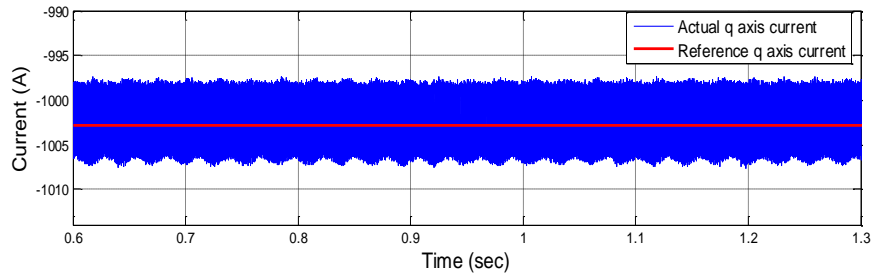


(a) Actual generator electrical angular speed vs. analytical value

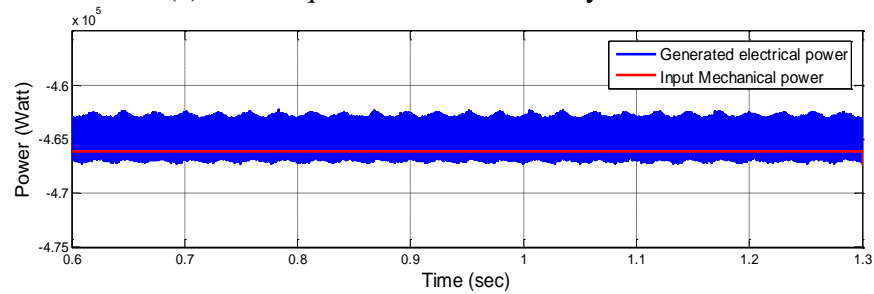
(b)



(b) Actual electromagnetic torque vs. analytical value

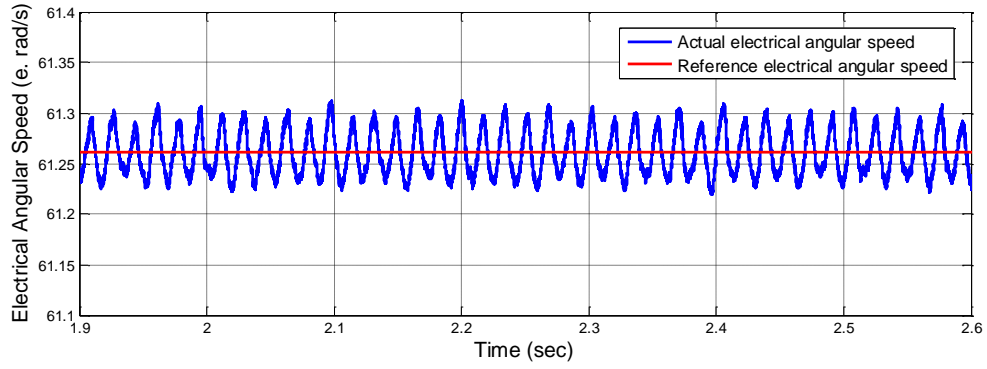


(c) Actual q -axis current vs. analytical value

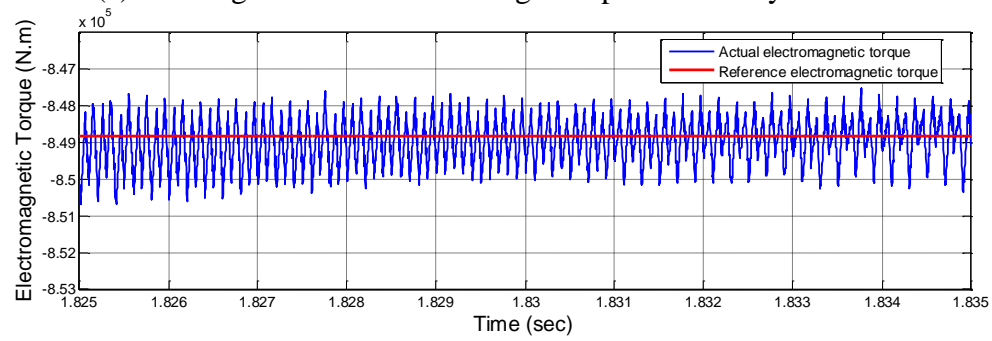


(d) Actual generated electrical power vs. input mechanical power

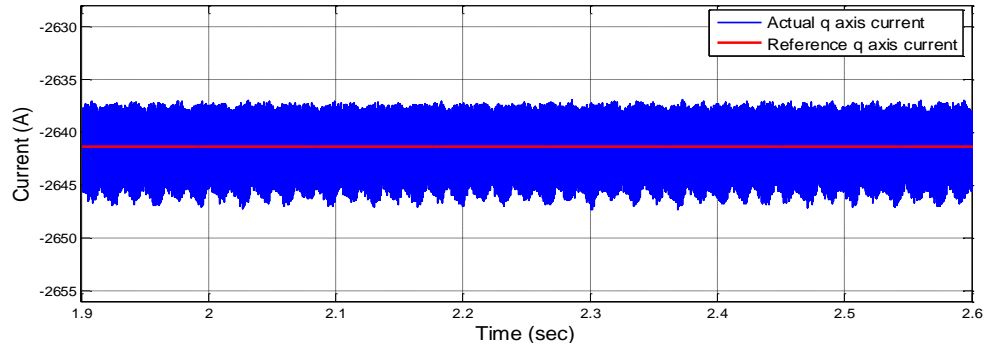
Figure 3.16 System Parameters in Static States with Wind Speed of $8m/s$



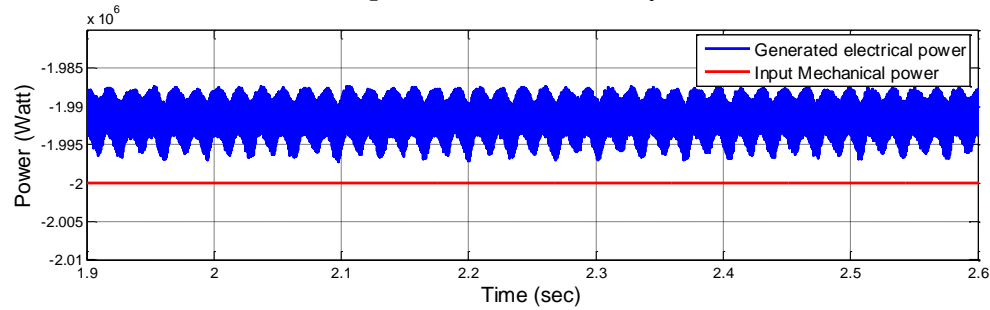
(a) Actual generator electrical angular speed vs. analytical value



(b) Actual electromagnetic torque vs. analytical value



(c) Actual q -axis current vs. analytical value



(d) Actual generated electrical power vs. input mechanical power

Figure 3.17 System parameters in static states with wind speed of 13m/s

Based on the simulation results and the analysis above, optimal power is generated by the PMSG wind turbine system at different wind speed levels. The chosen control algorithms applied in the control system of the generator-side converter are hence verified.

Chapter 4: Control of Grid-Side Converter

In direct-drive PMSG wind turbine systems, grid-connected converters play an important role in transforming the DC power to AC power. As introduced earlier in Chapter 3, there are three system variables that need to be strictly controlled. Namely, these variables are the speed of the PMSG, the DC bus voltage, and the complex power (active and reactive power) injected into the grid [6]. As the generator-side converter controls the speed of the PMSG, the grid-side converter regulates the DC bus voltage while controlling the active power and reactive power injected into the grid.

In this chapter, the control approach for the grid-side converter is analyzed. This converter is assumed to be operating on the basis of the principle of the space vector pulse width modulation (SVPWM), which will be elaborated on here. Furthermore, the simulation results will be obtained and given here to validate the proposed control strategy.

4.1 Grid-Side Converter Control based on Voltage Oriented Control

The simplified system topology of the direct-drive PMSG wind generation system is shown in Figure 4.1. In this figure, i_{ag} , i_{bg} , and i_{cg} , are the grid currents, their directions are defined by the arrows as shown in the figure. Thus, following the consumer/load notation in circuits, when the grid currents are positive, it means that the electrical power flows from the grid to the wind turbine system. Conversely, when the grid currents are negative, the power is injected into the grid from the wind generation

system. In the normal operating conditions of the system, the grid currents are always negative.

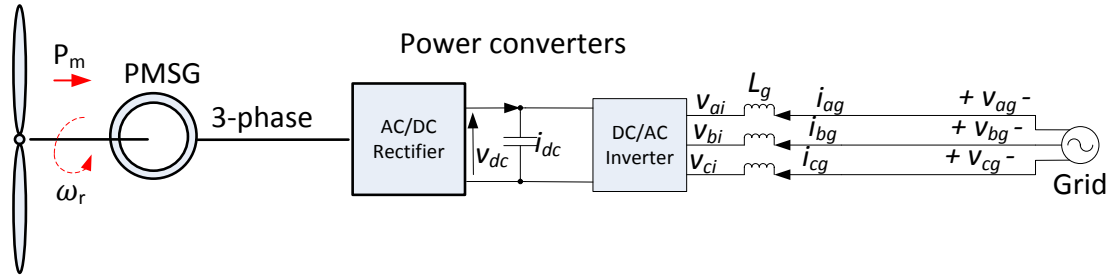


Figure 4.1 Simplified topology of the direct-drive PMSG wind generation system

As stated earlier, the main objective of the grid-side converter control is to regulate the active and reactive power. The expressions of the active power and reactive power injected into this grid can be written as follows, see [6]:

$$P_g = \frac{3}{2}(v_{dg}i_{dg} + v_{qg}i_{qg}) \quad (4.1)$$

$$Q_g = \frac{3}{2}(v_{qg}i_{dg} - v_{dg}i_{qg}) \quad (4.2)$$

where, i_{dg} and i_{qg} , are the grid currents in dq -axes reference frame, v_{dg} and v_{qg} , are the grid voltages in dq -axes reference frame. As can be seen in expressions (4.1) and (4.2), the d -axis and q -axis components of the grid currents and voltages are coupled in cross-product fashion in the reactive power term, which makes the active power and reactive power hard to control, and decreases the dynamic performance of the grid-side converter control. Based on this coupling issue, the voltage oriented control (VOC) approach is applied as the grid-side converter control algorithm. The VOC approach is implemented

here in the grid voltage synchronous reference frame, the d -axis of the rotating reference frame is aligned with the rotating grid voltage space vector. Accordingly, the q -axis component of the grid voltage space vector is equal to zero. The phasor diagram of the VOC approach is shown in Figure 4.2.

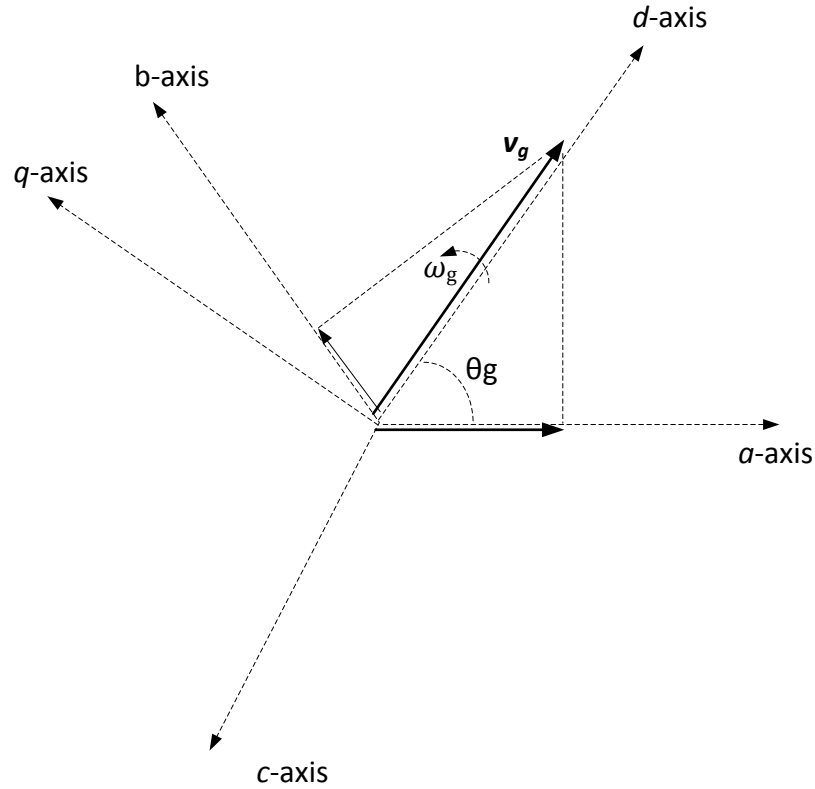


Figure 4.2 Phasor diagram of the VOC

With the application of the VOC approach, the expressions of the active and reactive power of equations (4.1) and (4.2) can be rewritten as follows:

$$P_g = \frac{3}{2} v_{dg} i_{dg} = v_{dc} i_{dc} \quad (4.3)$$

$$Q_g = -\frac{3}{2}v_{dg}i_{qg} \quad (4.4)$$

where, v_{dc} and i_{dc} , are the voltage and current of the dc bus, respectively. From equations (4.3) and (4.4), it can be observed that the active and reactive power can be controlled independently by the d -axis and q -axis components of the grid currents, respectively. The control scheme of the grid-side converter is shown in Figure 4.3.

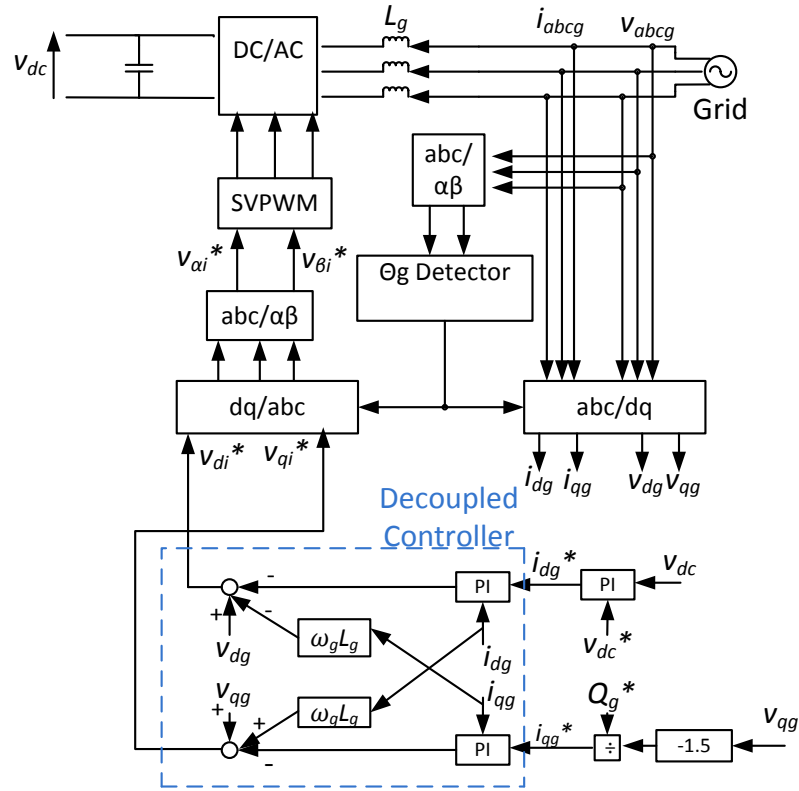


Figure 4.3 Control scheme of the grid-side converter

4.2 Space Vector Pulse Width Modulation

A voltage source inverter (VSI) is commonly used to transform the DC power to AC power with the ability to regulate the magnitude and frequency of the AC outputs. The sinusoidal pulse width modulation (SPWM) approach and the space vector pulse width modulation (SVPWM) approach are two of the most commonly used modulation methods for such VSIs. In the SPWM approach, three sinusoidal modulation signals are compared with a triangular carrier signal to generate the PWM pulses [45]. Compared to the SVPWM approach, the SPWM approach possesses the merits that it requires less computation effort and is easier to implement. However, the SPWM approach also has the drawbacks that it generates more harmonics in the AC outputs and requires higher DC bus voltage than that of the SVPWM approach to generate the same ac side voltage magnitudes. In the SVPWM approach, the reference signals are modified according to the operating conditions of the system in every sampling period, which can greatly improve the power quality of the AC outputs, that is, lower harmonic distortion [46]. This section will present the principles and implementation of the SVPWM approach.

4.2.1 Switching States

A typical voltage source inverter (VSI) is shown in Figure 4.4. In this figure, Q_1 through Q_6 , are the IGBT power switches, which are controlled by the switching signals, a , a' , b , b' , c and c' to set the "ON" and "OFF" states, respectively. Let one define that when the upper bridge switches (Q_1 , Q_2 and Q_3) are switched on ($a=b=c=1$), where the lower bridge switches (Q_4 , Q_5 and Q_6) will be switched off ($a'=b'=c'=0$), and vice versa. The upper and lower power switches for a given phase can never be switched on simultaneously in three-phase two level VSIs.

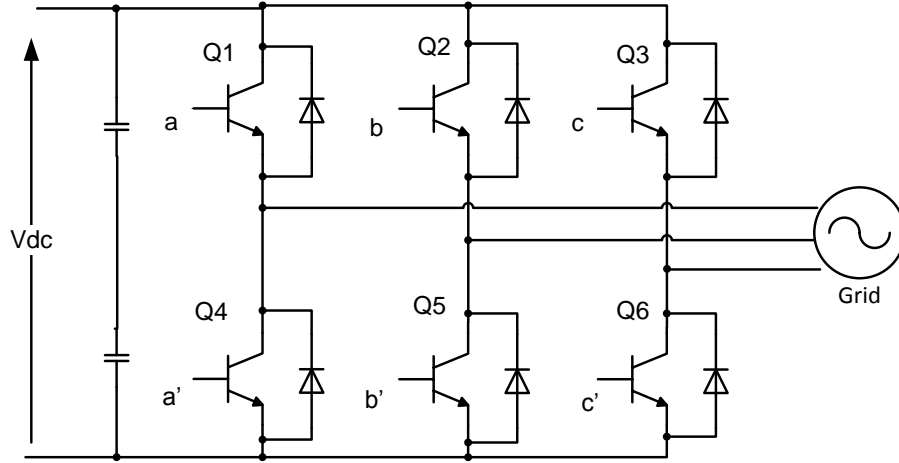


Figure 4.4 Two level voltage source inverter

The relationship between the switching vector, $[a \ b \ c]^T$, and the corresponding phase voltage vector can be expressed as follows [6]:

$$\begin{bmatrix} V_{an} \\ V_{bn} \\ V_{cn} \end{bmatrix} = \frac{1}{3} V_{dc} \begin{bmatrix} 2 & -1 & -1 \\ -1 & 2 & -1 \\ -1 & -1 & 2 \end{bmatrix} \begin{bmatrix} a \\ b \\ c \end{bmatrix} \quad (4.5)$$

where, V_{an} , V_{bn} and V_{cn} , are the magnitudes of the three-phase line-to-neutral voltages of the VSI, and, V_{dc} , is the DC bus voltage. Here, a , b and c , are the switching signals (0 or 1) of the IGBTs. Again, the relationship between the switching vector, $[a \ b \ c]^T$, and the line-to-line voltages of the VSI can accordingly be expressed as [6]:

$$\begin{bmatrix} V_{ab} \\ V_{bc} \\ V_{ca} \end{bmatrix} = \frac{1}{3} V_{dc} \begin{bmatrix} 1 & -1 & 0 \\ 0 & 1 & -1 \\ -1 & 0 & 1 \end{bmatrix} \begin{bmatrix} a \\ b \\ c \end{bmatrix} \quad (4.6)$$

where, V_{ab} , V_{bc} and V_{ca} , are the magnitudes of the three-phase line-to-line voltages of the VSI. According to expressions (4.5) and (4.6), for different switching states, the values of the line-to-neutral voltages and line-to-line voltages of the VSI can be expressed as given

in Table 4.1. In this table, when the switching vector, $[a \ b \ c]^T = [1 \ 1 \ 1]^T$ or $[0 \ 0 \ 0]^T$, it means that the three-phase terminal of the VSI are shorted by turning on all the upper or lower switches, denoted as zero states. Thus, the operation of the inverter has six active states and two zero states.

Table 4.1 Switching states and output voltages of the VSI

Switching States			Line to Neutral Voltages			Line to Line Voltages		
a	b	c	V_{an}	V_{bn}	V_{cn}	V_{ab}	V_{bc}	V_{ca}
0	0	0	0	0	0	0	0	0
1	0	0	$\frac{2}{3}V_{dc}$	$-\frac{1}{3}V_{dc}$	$-\frac{1}{3}V_{dc}$	V_{dc}	0	$-V_{dc}$
0	1	0	$-\frac{1}{3}V_{dc}$	$\frac{2}{3}V_{dc}$	$-\frac{1}{3}V_{dc}$	$-V_{dc}$	V_{dc}	0
1	1	0	$\frac{1}{3}V_{dc}$	$\frac{1}{3}V_{dc}$	$-\frac{2}{3}V_{dc}$	0	V_{dc}	$-V_{dc}$
0	0	1	$-\frac{1}{3}V_{dc}$	$-\frac{1}{3}V_{dc}$	$\frac{2}{3}V_{dc}$	0	$-V_{dc}$	V_{dc}
1	0	1	$\frac{1}{3}V_{dc}$	$-\frac{2}{3}V_{dc}$	$\frac{1}{3}V_{dc}$	V_{dc}	$-V_{dc}$	0
0	1	1	$-\frac{2}{3}V_{dc}$	$\frac{1}{3}V_{dc}$	$\frac{1}{3}V_{dc}$	$-V_{dc}$	0	V_{dc}
1	1	1	0	0	0	0	0	0

4.2.2 Space Vectors

Before analyzing the principles of the SVPWM approach, the concept of space vectors needs to be introduced first. As stated earlier, the objective of the SVPWM approach is to generate the balanced three-phase voltage outputs for the VSI, assuming that the phase voltages of the VSI are three-phase sinusoidal waveforms and can be expressed as follows:

$$v_{an} = V_m \cos \omega t \quad (4.7)$$

$$v_{bn} = V_m \cos(\omega t - \frac{2\pi}{3}) \quad (4.8)$$

$$v_{cn} = V_m \cos(\omega t + \frac{2\pi}{3}) \quad (4.9)$$

where, V_m , is the peak magnitude of the phase voltages, and, ω , is the electrical angular frequency/speed of the voltage space vector. According to Clarke's transformation [41], the line-to-neutral voltages in the three-phase stationary reference frame can be transformed to a two-phase stationary reference frame through the following expression:

$$\begin{bmatrix} v_\alpha \\ v_\beta \end{bmatrix} = \frac{2}{3} \begin{bmatrix} 1 & -\frac{1}{2} & -\frac{1}{2} \\ 0 & \frac{\sqrt{3}}{2} & -\frac{\sqrt{3}}{2} \end{bmatrix} \begin{bmatrix} v_{an} \\ v_{bn} \\ v_{cn} \end{bmatrix} \quad (4.10)$$

where, v_α and v_β , are the α -axis and β -axis component of the VSI output voltage vector.

Substituting expression (4.5) into (4.10), expression (4.10) can be rewritten as follows:

$$\begin{bmatrix} v_\alpha \\ v_\beta \end{bmatrix} = \frac{2}{3} V_{dc} \begin{bmatrix} 1 & -\frac{1}{2} & -\frac{1}{2} \\ 0 & \frac{\sqrt{3}}{2} & -\frac{\sqrt{3}}{2} \end{bmatrix} \begin{bmatrix} a \\ b \\ c \end{bmatrix} \quad (4.11)$$

From expression (4.11), by varying the switching vector, $[a \ b \ c]^T$, the α -axis and β -axis voltages can be obtained for the various states. For example, when $[a \ b \ c]^T = [1 \ 0 \ 0]$, the α -axis and β -axis voltage vector, $[v_\alpha \ v_\beta] = [\frac{2}{3}V_{dc} \ 0]$, the space vector which corresponds to this switching state is V_1 as shown in Figure 4.5. Shown in Table 4.2 are the VSI output phase voltage space vectors corresponding to the different switching states.

Table 4.2 VSI phase voltage space vectors correspond to different switching states

Switching States			Voltage Space Vector $\alpha\beta$ -axes Components		Vectors Definition
a	b	c	v_α	v_β	Vectors
0	0	0	0	0	$V_0 (0 \ 0 \ 0)$
1	0	0	$\frac{2}{3}V_{dc}$	0	$V_1 (1 \ 0 \ 0)$
0	1	0	$-\frac{1}{3}V_{dc}$	$\frac{1}{\sqrt{3}}V_{dc}$	$V_3 (0 \ 1 \ 0)$
1	1	0	$\frac{1}{3}V_{dc}$	$\frac{1}{\sqrt{3}}V_{dc}$	$V_2 (1 \ 1 \ 0)$
0	0	1	$-\frac{1}{3}V_{dc}$	$-\frac{1}{\sqrt{3}}V_{dc}$	$V_5 (0 \ 0 \ 1)$
1	0	1	$\frac{1}{3}V_{dc}$	$-\frac{1}{3}V_{dc}$	$V_6 (1 \ 0 \ 1)$
0	1	1	$-\frac{2}{3}V_{dc}$	0	$V_4 (0 \ 1 \ 1)$
1	1	1	0	0	$V_7 (1 \ 1 \ 1)$

According to Table 4.2, a typical space vector diagram for the two level VSI can be drawn, as shown in Figure 4.5. In this figure, the six active space vectors, V_1 through V_6 , form a hexagon with two zero space vectors, V_0 and V_7 , laying at the central point (origin) of the hexagon. As can be seen in this figure, the hexagon is separated evenly by the active space vectors to six equilateral triangles.

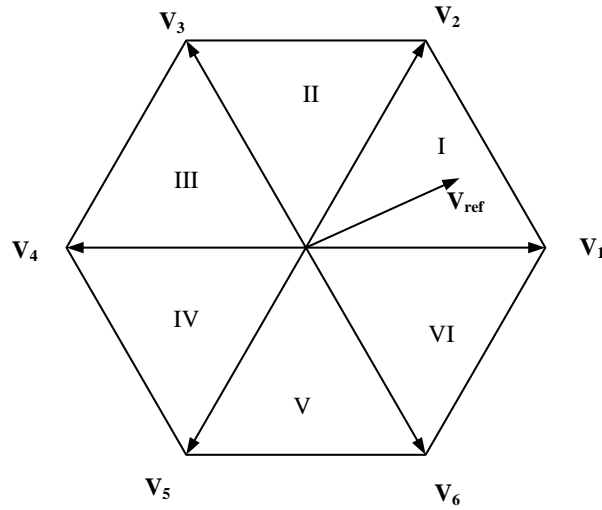


Figure 4.5 Voltage space vector diagram for the two level VSI

Assuming that the commanded phase voltages of the VSI are sinusoidal three-phase balanced voltages, they will constitute a reference voltage space vector, V_{ref} , which rotates at an angular velocity, $\omega = 2\pi f$, where, f , is the fundamental frequency of the phase voltages of the VSI.

4.2.3 Implementation of the SVPWM

As introduced earlier, the objective of the SVPWM method is to approximate the reference voltage vector, V_{ref} , by properly turning the power switches of the VSI "ON" or "OFF". Here, it is assumed that the sampling time, T_s , is small enough such that the reference voltage space vector can be regarded as constant during the sampling time. Thus, the reference voltage space vector, V_{ref} , can be synthesized by its adjacent active space vectors and zero space vectors [6]. Based on the analysis above, when given the reference voltages, the process of implementing the SVPWM approach can be divided into the following steps:

1. Determine the amplitude of the voltage space vector and its angle;
2. Determine which sector is the voltage space vector in;
3. Calculate the dwell time of the adjacent switch voltage space vectors to synthesize the reference voltage space vector.

4.2.3.1 Determination of the voltage space vector

In every sampling time, the reference three-phase line-to-neutral voltages are sent to the SVPWM module as the input signals. Thus, the voltage space vector can be achieved by transforming the three-phase line-to-neutral voltages into $\alpha\beta$ -axes reference frame based on expression (4.10). Consequently, the α -axis and β -axis voltage components, v_α and v_β , can be expressed as follows:

$$v_\alpha = v_{an} - \frac{1}{2}v_{bn} - \frac{1}{2}v_{cn} \quad (4.12)$$

$$v_{\beta} = \frac{\sqrt{3}}{2} v_{bn} - \frac{\sqrt{3}}{2} v_{cn} \quad (4.13)$$

Based on expressions (4.12) and (4.13), the magnitude and the angle of the voltage space vector can be expressed as follows:

$$|V_{ref}| = \sqrt{v_{\alpha}^2 + v_{\beta}^2} \quad (4.14)$$

$$\theta = \tan^{-1}\left(\frac{v_{\alpha}}{v_{\beta}}\right) \quad (4.15)$$

4.2.3.2 Determination of the location of the reference voltage space vector

As stated earlier, the reference voltage space vector is rotating in space with an angular frequency of ω . In order to properly select the adjacent active space vectors to synthesize the reference voltage space vector, one needs to determine the location of the reference voltage space vector first, that is, which sector is the voltage space vector in. As shown in Figure 4.5, the hexagon formed by the six active space vectors are separated into six equilateral triangles, denoted as sector I through VI. In the SVPWM approach, the combination of the adjacent space vectors to choose to synthesize the reference voltage space vector is dependent on which sector the reference voltage space vector is in. For example, when the rotating reference voltage space vector is in sector I ($0 \leq \theta < 60^\circ$), the adjacent switching state voltage vectors, V_1 , V_2 and V_0 , are chosen to synthesize the reference voltage space vector. Table 4.3 shows the angle of the reference voltage space vector and the combination of adjacent space vectors when the reference voltage space vector is in other sectors.

Table 4.3 Determination of the location of the reference voltage space vector

Location of the Reference Voltage Space Vector	Angle of the Reference Voltage Space Vector	Combination of the Switch State Voltage Vector to Synthesized the Reference
Sector I	$0^\circ \leq \theta < 60^\circ$	V_1, V_2 and zero vector
Sector II	$60^\circ \leq \theta < 120^\circ$	V_2, V_3 and zero vector
Sector III	$120^\circ \leq \theta < 180^\circ$	V_3, V_4 and zero vector
Sector IV	$180^\circ \leq \theta < 240^\circ$	V_4, V_5 and zero vector
Sector V	$240^\circ \leq \theta < 300^\circ$	V_5, V_6 and zero vector
Sector VI	$300^\circ \leq \theta < 360^\circ$	V_6, V_1 and zero vector

4.2.3.3 Dwell time calculation

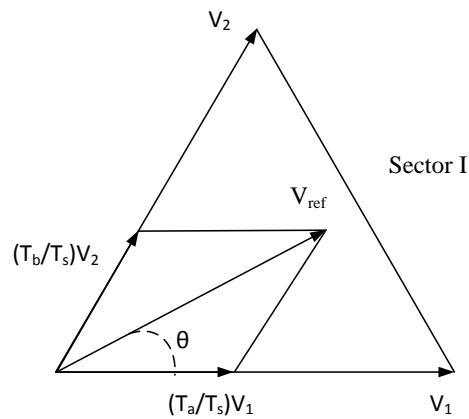


Figure 4.6 Dwell time calculation diagram when the reference voltage vector is in sector I [6]

It is known that a reference voltage space vector can be synthesized by three stationary adjacent space vectors in each sector. The term, dwell time, indicates how long the corresponding power switches will be turned on during a sampling time, T_s . For example, when the reference voltage space vector, V_{ref} , is in sector I, as shown in Figure 4.6, the space vectors, V_1 , V_2 and the zero vectors are selected as the adjacent vectors to synthesize this reference voltage vector, V_{ref} . In this figure, T_a , T_b and T_0 are the dwell times for the space vectors, V_1 , V_2 and the zero vectors, respectively. If the sampling time, T_s , is sufficiently small, according to volt-second balancing principle [6], we have:

$$V_{ref}T_s = V_1T_a + V_2T_b + V_{0/7}T_0 \quad (4.16)$$

$$T_s = T_a + T_b + T_0 \quad (4.17)$$

In expression (4.16), the left term, $V_{ref}T_s$, can be divided into an α -axis component and a β -axis component, which can be expressed as follows:

$$\alpha\text{-axis} \quad V_{ref}T_s \cos(\theta) = V_1T_a + V_2T_b = \frac{2}{3}V_{dc}T_a + \frac{1}{3}V_{dc}T_b \quad (4.18)$$

$$\beta\text{-axis} \quad V_{ref}T_s \sin(\theta) = \frac{\sqrt{3}}{3}V_{dc}T_b \quad (4.19)$$

Solving expressions (4.17), (4.18) and (4.19), the dwell time for the space vectors, V_1 , V_2 and the zero vectors can be expressed as follows:

$$T_a = \frac{\sqrt{3}T_s v_{ref}}{V_{dc}} \sin\left(\frac{\pi}{3} - \theta\right) \quad (4.20)$$

$$T_b = \frac{\sqrt{3}T_s v_{ref}}{V_{dc}} \sin(\theta) \quad (4.21)$$

$$T_0 = T_s - T_a - T_b \quad (4.22)$$

Although the dwell time calculation process above is for the reference voltage space vector, V_{ref} , in sector I, it can also be applied when the reference vector is in any of the other sectors by modifying the voltage space vector angle, θ , based on the following expression [6]:

$$\theta' = \theta - (k - 1) \frac{\pi}{3} \quad (4.23)$$

where, k , is the sector number, and, θ' , is the modified voltage space vector angle within the range of 0 to $\pi/3$. Since the dwell time of the switching state voltage space vectors has been calculated, the next step is to define the switching sequence. Shown in Figure 4.7 is the most commonly applied seven segments switching sequence when the reference voltage vector is in sector I. The seven segments switching sequence has the advantages that it generates low power losses on the power switches (IGBTs) and it contributes to a low THD in the output voltages of the VSI. The switching sequences for the reference voltage vector when it is in other sectors are shown in Table 4.4.

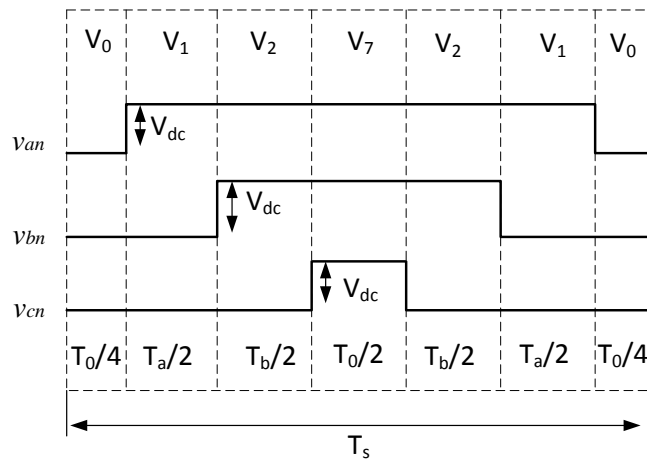


Figure 4.7 Seven-segment switching sequence of the SVPWM for sector I

Table 4.4 Seven segment switching sequence

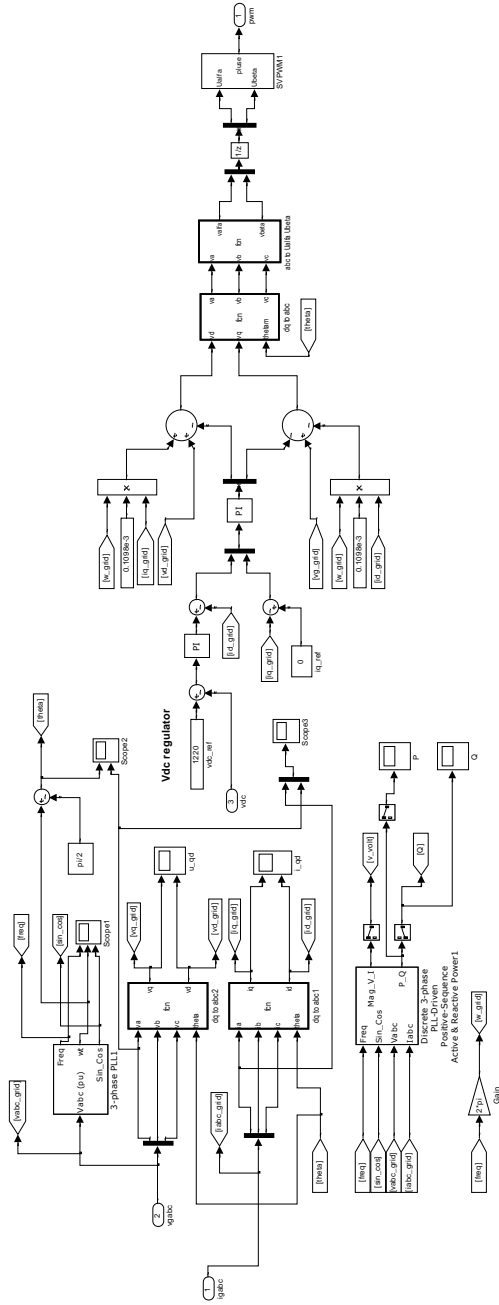
Sect or	Switching Segment						
	1 $(\frac{T_0}{4})$	2 $(\frac{T_a}{2})$	3 $(\frac{T_b}{2})$	4 $(\frac{T_0}{2})$	5 $(\frac{T_b}{2})$	6 $(\frac{T_a}{2})$	7 $(\frac{T_0}{4})$
I	$V_0 (0\ 0\ 0)$	$V_1 (1\ 0\ 0)$	$V_2 (1\ 1\ 0)$	$V_7 (1\ 1\ 1)$	$V_2 (1\ 1\ 0)$	$V_1 (1\ 0\ 0)$	$V_0 (0\ 0\ 0)$
II	$V_0 (0\ 0\ 0)$	$V_3 (0\ 1\ 0)$	$V_2 (1\ 1\ 0)$	$V_7 (1\ 1\ 1)$	$V_2 (1\ 1\ 0)$	$V_3 (0\ 1\ 0)$	$V_0 (0\ 0\ 0)$
III	$V_0 (0\ 0\ 0)$	$V_3 (0\ 1\ 0)$	$V_4 (0\ 1\ 1)$	$V_7 (1\ 1\ 1)$	$V_4 (0\ 1\ 1)$	$V_3 (0\ 1\ 0)$	$V_0 (0\ 0\ 0)$
IV	$V_0 (0\ 0\ 0)$	$V_5 (0\ 0\ 1)$	$V_4 (0\ 1\ 1)$	$V_7 (1\ 1\ 1)$	$V_4 (0\ 1\ 1)$	$V_5 (0\ 0\ 1)$	$V_0 (0\ 0\ 0)$
V	$V_0 (0\ 0\ 0)$	$V_5 (0\ 0\ 1)$	$V_6 (1\ 0\ 1)$	$V_7 (1\ 1\ 1)$	$V_6 (1\ 0\ 1)$	$V_5 (0\ 0\ 1)$	$V_0 (0\ 0\ 0)$
VI	$V_0 (0\ 0\ 0)$	$V_1 (1\ 0\ 0)$	$V_6 (1\ 0\ 1)$	$V_7 (1\ 1\ 1)$	$V_6 (1\ 0\ 1)$	$V_1 (1\ 0\ 0)$	$V_0 (0\ 0\ 0)$

4.3 Simulation Results and Analysis

The simulation parameters and operating conditions are the same as for the control of the generator-side converter, which is shown in Table 3.1. The circuit diagram of the system implemented in MATLAB/Simulink is shown in Figure 3.7, and the control scheme of the grid-side control system is shown in Figure 4.8. The simulation results of the grid-side control are shown in Figures 4.9 through 4.13.

Shown in Figure 4.9 are the grid voltages with a constant magnitude of 690V line-to-line (60Hz). As analyzed earlier in Chapter 3, the power generated by the PMSG is proportional to the wind speed (below the rated wind speed of the system). When the grid voltages are set at constant magnitude and frequency under normal operating conditions,

the grid currents are also proportion to the wind speed. This can be seen in Figure 4.10. The grid currents in the dq-axes reference frame are shown in Figures 4.11 and 4.12. In order to achieve the unity power factor on the grid-side control, the q-axis current is forced to zero. Thus, the magnitude of the d-axis current is equal to that of the grid current space vector, as shown in Figure 4.11. The active power and reactive power injected into the grid are shown in Figure 4.13. From this figure, the reactive power is kept at zero, based on the unity power factor control, and the active power which is controlled by the d-axis current is proportional to the wind speed. Under rated load condition, the active power is slightly lower than 2 MW, this is due to the internal power losses. Based on the analysis above, the control objectives of the grid-side converter have been achieved.



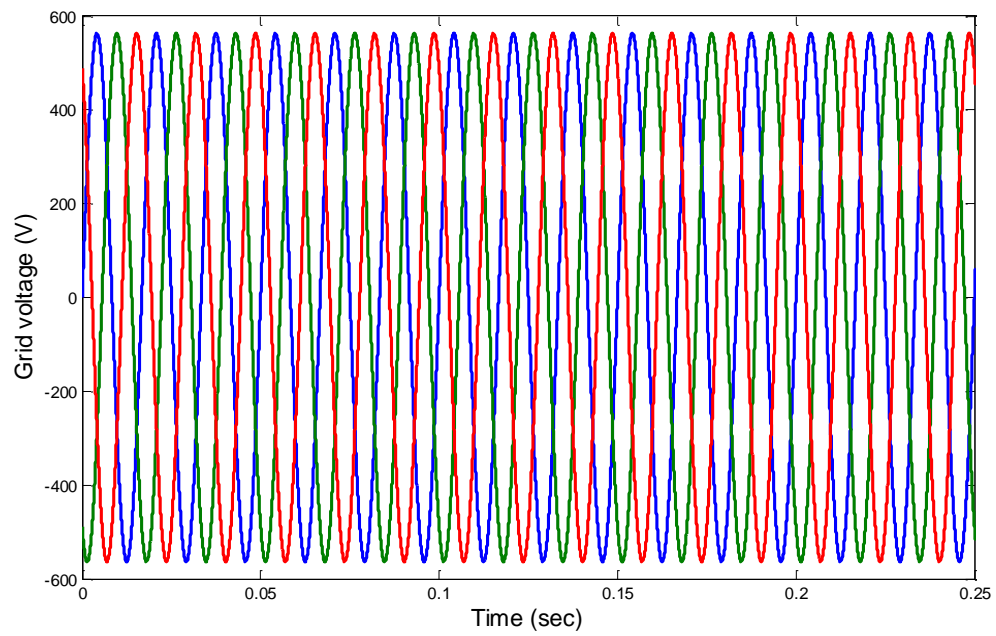


Figure 4.9 Grid voltages of the system

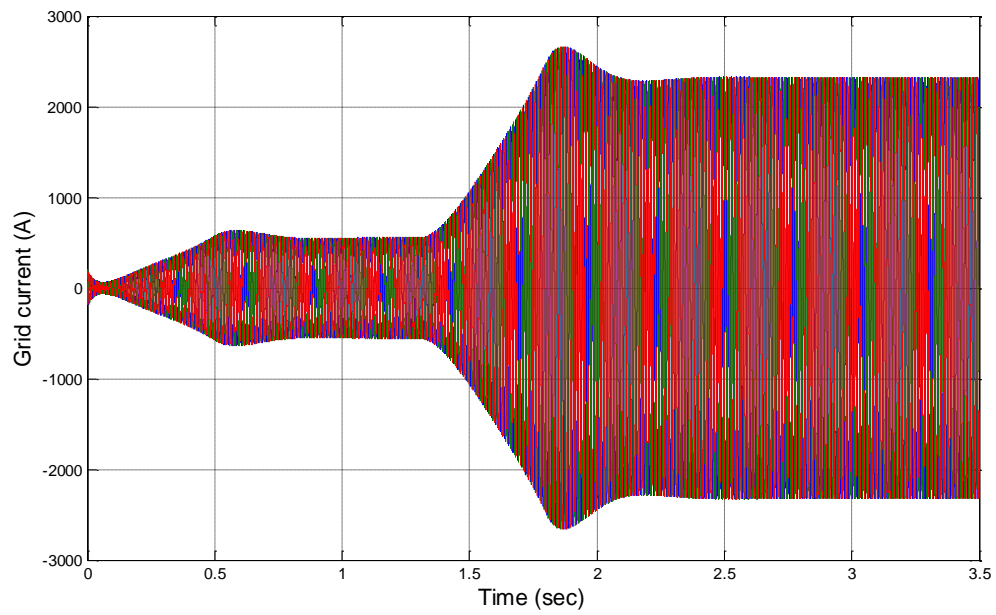


Figure 4.10 Grid currents of the system

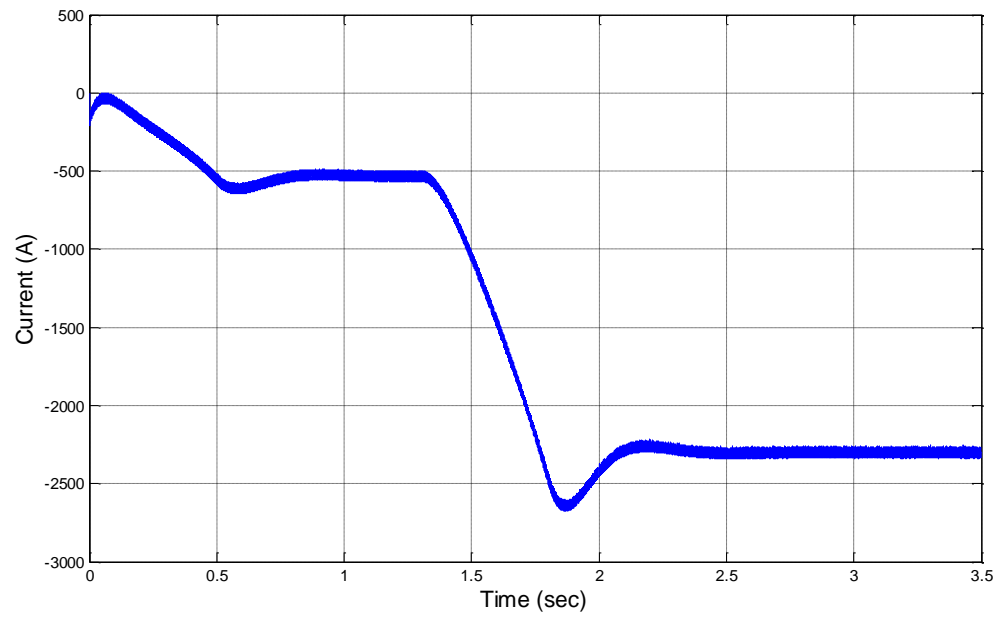


Figure 4.11 The d-axis component of the grid current

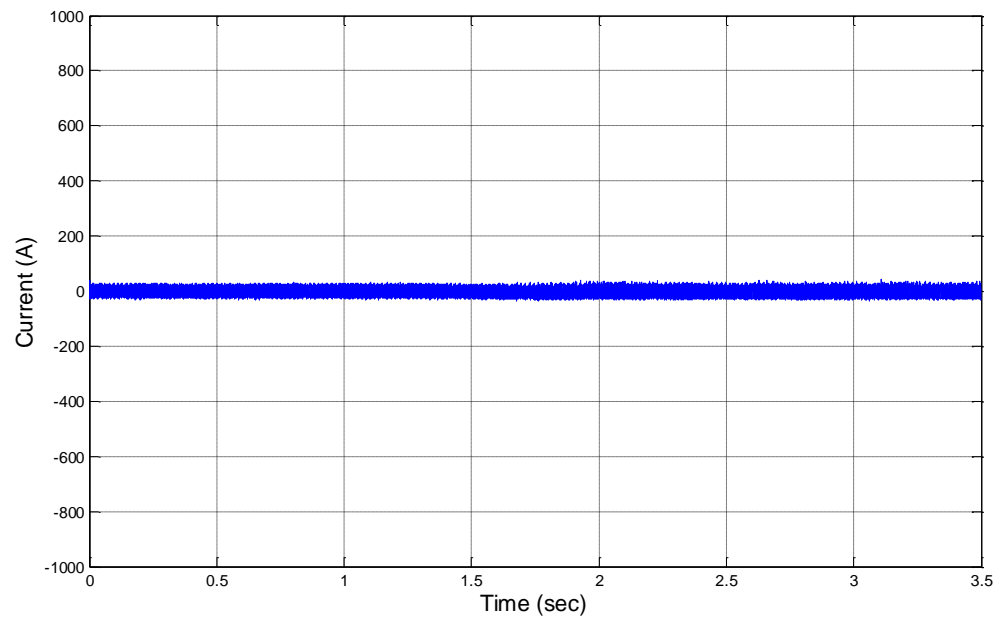


Figure 4.12 The q-axis component of the grid current

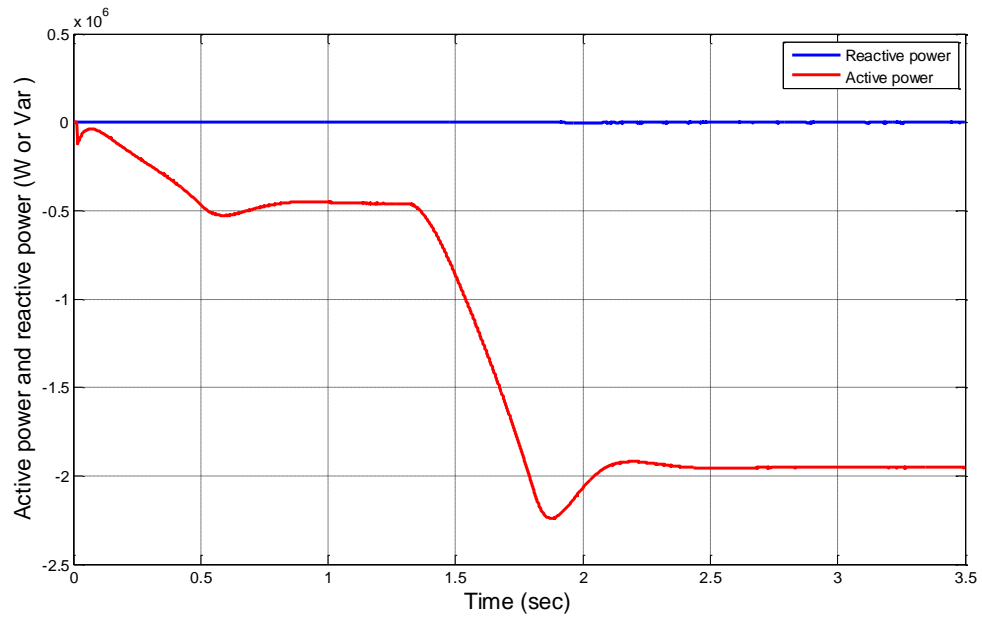


Figure 4.13 The active and reactive power injected into the grid

Chapter 5: Sliding Mode Observer based Rotor Position and Speed Sensorless Control

As introduced earlier in Chapter 3, the implementation of the FOC approach needs the rotor position and speed information of the PMSG. The speed of the rotor is needed to set up the speed feedback loop for the FOC approach, while the information of the rotor position is the prerequisite to perform the coordinate transformation. Conventional methods to achieve the rotor position information are usually based on an encoder or transducer mounted on the rotor shaft. However, the presence of such electrical sensors reduces the reliability of the system, and the failure of the rotor shaft speed sensor will cause the malfunction of the whole system, which results in a significant reduction of the power production of the wind turbine generator system. Based on this issue, a sliding mode observer (SMO) based PMSG rotor position and speed sensorless control strategy will be presented in this chapter in order to eliminate the presence of the rotor shaft speed sensor. In this chapter, the principle of the sliding mode control algorithm will be analyzed, and the simulation results will be given to validate the speed sensorless control algorithm.

5.1 Sliding Mode Control

In Chapter 2, the voltage functions of the PMSM in the dq -axes reference frame were expressed as follows:

$$v_{ds} = R_s i_{ds} + L_d \frac{di_{ds}}{dt} - \omega_e L_q i_{qs} \quad (2.12)$$

$$v_{qs} = R_s i_{qs} + L_q \frac{di_{qs}}{dt} + \omega_e L_d i_{ds} + \omega_e \lambda_r \quad (2.13)$$

Transforming the voltage functions into the $\alpha\beta$ -axes reference frame, the state space functions of the PMSM can be rewritten as follows:

$$\frac{di_{\alpha s}}{dt} = -\frac{R_s}{L_s} i_{\alpha s} - \frac{1}{L_s} e_{\alpha s} + \frac{1}{L_s} v_{\alpha s} \quad (5.1)$$

$$\frac{di_{\beta s}}{dt} = -\frac{R_s}{L_s} i_{\beta s} - \frac{1}{L_s} e_{\beta s} + \frac{1}{L_s} v_{\beta s} \quad (5.2)$$

where, $i_{\alpha s}$ and $i_{\beta s}$, are the stator currents in the $\alpha\beta$ -axes reference frame, and, $v_{\alpha s}$ and $v_{\beta s}$, are the stator voltages in the $\alpha\beta$ -axes reference frame. Here, $e_{\alpha s}$ and $e_{\beta s}$, are the $\alpha\beta$ -axes back EMFs which can be expressed as follows [34]:

$$e_{\alpha s} = -\lambda_r \omega_e \sin \theta_r \quad (5.3)$$

$$e_{\beta s} = \lambda_r \omega_e \cos \theta_r \quad (5.4)$$

where, ω_e , is the electrical angular speed of the rotor, while, λ_r , is the peak/maximum phase flux linkage due to the rotor-mounted PMs. As can be seen in equations (5.3) and (5.4), the back EMF contains the information of the rotor speed, ω_e , as well as the rotor angle, θ_r , which means that by estimating the back EMF, one will be able to obtain the information on the rotor position and speed. As introduced earlier, the sliding mode observer based rotor position and speed estimation method is back EMF based sensorless control. By building the sliding mode observer, one will be able to estimate the back EMF, further estimate the rotor position and speed.

According to the SMO theory [27], [28], [33], the sliding mode observer for the PMSG can be expressed as follows [31]:

$$\frac{di_{\alpha s}^{est}}{dt} = -\frac{R_s}{L_s}i_{\alpha s}^{est} + \frac{1}{L_s}v_{\alpha s} - k * sgn(i_{\alpha s}^{est} - i_{\alpha s}) \quad (5.5)$$

$$\frac{di_{\beta s}^{est}}{dt} = -\frac{R_s}{L_s}i_{\beta s}^{est} + \frac{1}{L_s}v_{\beta s} - k * sgn(i_{\beta s}^{est} - i_{\beta s}) \quad (5.6)$$

where, $i_{\alpha s}^{est}$ and $i_{\beta s}^{est}$, are the estimated values of the stator currents. Here, k , is the switching gain, while, $sgn(i_{\alpha s}^{est} - i_{\alpha s})$ and $sgn(i_{\beta s}^{est} - i_{\beta s})$, are the signum functions based on the error of the estimated stator currents and the actual stator currents. The property of the signum function can be expressed in Figure 5.1 and the following expression:

$$sgn(x) = \begin{cases} -1 & (x < 0) \\ 0 & (x = 0) \\ 1 & (x > 0) \end{cases} \quad (5.7)$$

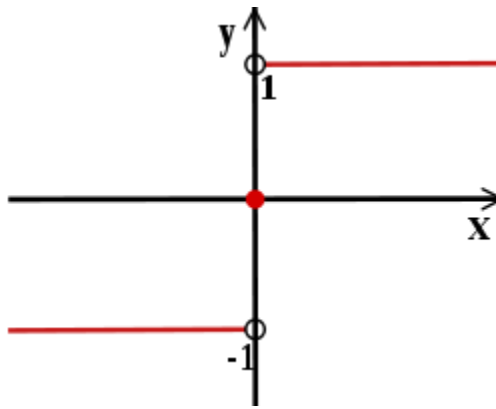


Figure 5.1 Operation properties of the signum function

Here, one defines the current error vector as:

$$\varepsilon_i(\alpha, \beta) = \begin{bmatrix} i_{\alpha s}^{est} \\ i_{\beta s}^{est} \end{bmatrix} - \begin{bmatrix} i_{\alpha s} \\ i_{\beta s} \end{bmatrix} \quad (5.8)$$

and one defines the back EMF error vector as:

$$\varepsilon_e(\alpha, \beta) = \begin{bmatrix} e_{\alpha s}^{est} \\ e_{\beta s}^{est} \end{bmatrix} - \begin{bmatrix} e_{\alpha s} \\ e_{\beta s} \end{bmatrix} \quad (5.9)$$

In this sliding mode observer, the sliding surface is defined by the following expression:

$$s(x) = \varepsilon_i(\alpha, \beta) = i_{\alpha\beta s}^{est} - i_{\alpha\beta s} = 0 \quad (5.10)$$

The sliding surface is actually the ideal state trajectory of the sliding mode observer that the estimated stator currents are equal to the actual stator currents. However, this ideal sliding mode exists only when the switching frequency is infinitely high. In actual systems, the finite switching frequency makes the operation of the observer oscillate within a neighborhood of the sliding surface [35]. This oscillation is called chattering. In the sliding mode observer in expression (5.5) and (5.6), the signum functions are the feedback inputs for the observer. The value of the feedback input is based on the error of the estimated stator currents and the actual stator currents. This means that in every sampling time, the estimated stator currents are compared with the actual stator currents, by sending their errors to the signum functions, which will output a proper feedback control signal to the observer to make sure that the observer is operating along the pre-defined sliding surface.

The sliding mode will occur only if the value of the switching gain, k , is high enough to meet the sliding mode condition which can be expressed as [36]:

$$s^T \frac{d s}{dt} = \varepsilon_i(\alpha, \beta)^T \cdot \frac{d}{dt} \varepsilon_i(\alpha, \beta) < 0 \quad (5.11)$$

When the sliding mode occurs, we have:

$$\varepsilon_i(\alpha, \beta) = \frac{d}{dt} \varepsilon_i(\alpha, \beta) = 0 \quad (5.12)$$

Let us make subtractions between the sliding mode observer expressions (expressions (5.5) and (5.6)) and the original state space function of the PMSG (expressions (5.1) and (5.2)), we have:

$$\frac{d}{dt} (i_{\alpha s}^{est} - i_{\alpha s}) = -\frac{R_s}{L_s} (i_{\alpha s}^{est} - i_{\alpha s}) - \frac{1}{L_s} (e_{\alpha s}^{est} - e_{\alpha s}) + Z_{\alpha} \quad (5.13)$$

$$\frac{d}{dt} (i_{\beta s}^{est} - i_{\beta s}) = -\frac{R_s}{L_s} (i_{\beta s}^{est} - i_{\beta s}) - \frac{1}{L_s} (e_{\beta s}^{est} - e_{\beta s}) + Z_{\beta} \quad (5.14)$$

where, $Z_{\alpha} = -k * \text{sgn}(i_{\alpha s}^{est} - i_{\alpha s})$ and $Z_{\beta} = -k * \text{sgn}(i_{\beta s}^{est} - i_{\beta s})$, which are denoted as the switching functions. When the sliding mode occurs, substituting equation (5.12) into expressions (5.13) and (5.14), we have:

$$\frac{1}{L_s} (e_{\alpha s}^{est} - e_{\alpha s}) = Z_{\alpha} \quad (5.15)$$

$$\frac{1}{L_s} (e_{\beta s}^{est} - e_{\beta s}) = Z_{\beta} \quad (5.16)$$

Form expressions (5.15) and (5.16), the switching functions contain the information of the back EMFs, a typical method to achieve the estimated back EMFs is to apply a low-pass filter at the output of the switching functions [31], which can be expressed as:

$$e_{\alpha s}^{est} = \frac{\omega_{cutoff}}{s + \omega_{cutoff}} * Z_{\alpha s} \quad (5.17)$$

$$e_{\beta s}^{est} = \frac{\omega_{cutoff}}{s + \omega_{cutoff}} * Z_{\beta s} \quad (5.18)$$

Where, ω_{cutoff} , is the cutoff frequency of the low-pass filter. Thus, the estimated rotor position angle, θ_r^{est} , can be expressed as follows:

$$\theta_r^{est} = -\tan^{-1}\left(\frac{e_{\alpha}^{est}}{e_{\beta}^{est}}\right) \quad (5.19)$$

The phase angle shift due to the low-pass filter can be expressed as follows [37]:

$$\Delta\theta_r = \tan^{-1}\left(\frac{\omega_e}{\omega_{cutoff}}\right) \quad (5.20)$$

Where, $\Delta\theta_r$, is the rotor position angle compensation. The block diagram of the sliding mode observer is shown in Figure 5.2, and the control scheme of the whole system including the sliding mode observer is shown in Figure 5.3.

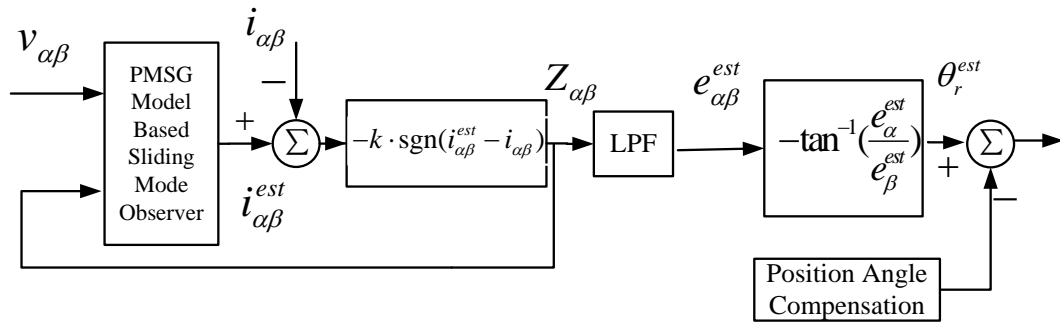


Figure 5.2 Block diagram of the sliding mode observer

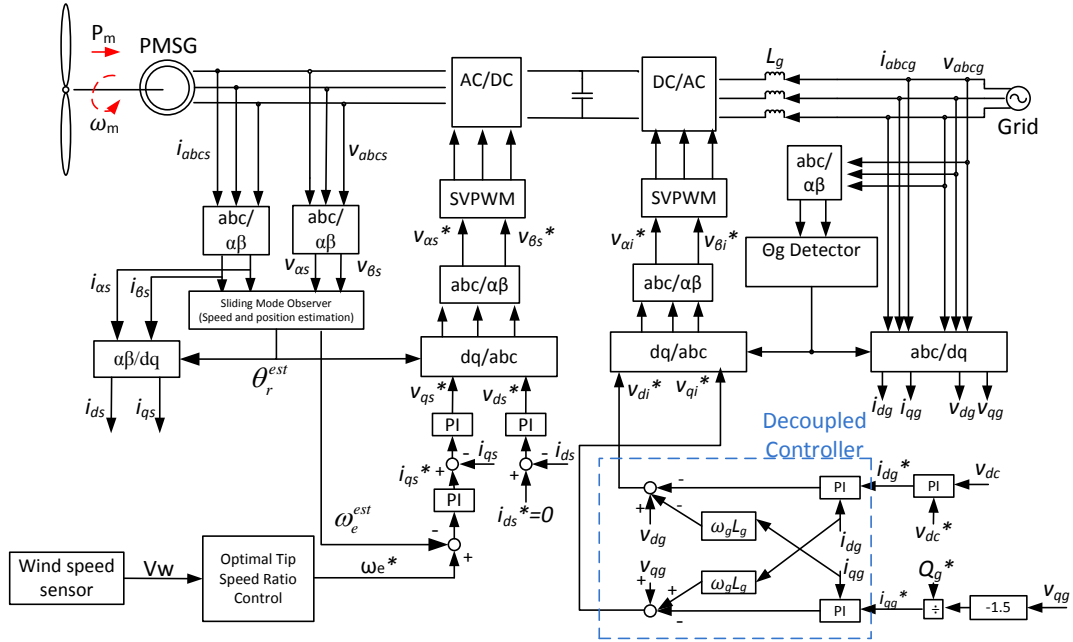


Figure 5.3 Control scheme of the wind turbine generation system including the sliding mode observer

5.2 Simulation Results and Analysis

The simulation parameters and operation conditions are shown in Table 3.1. The simulation results are shown in Figure 5.4 through 5.7.

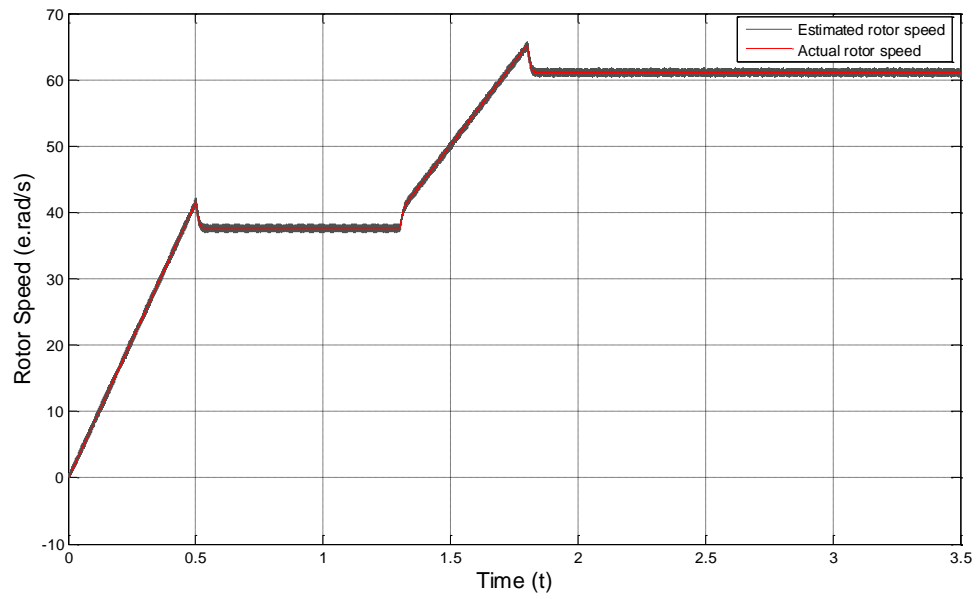


Figure 5.4 Estimated and actual rotor speed

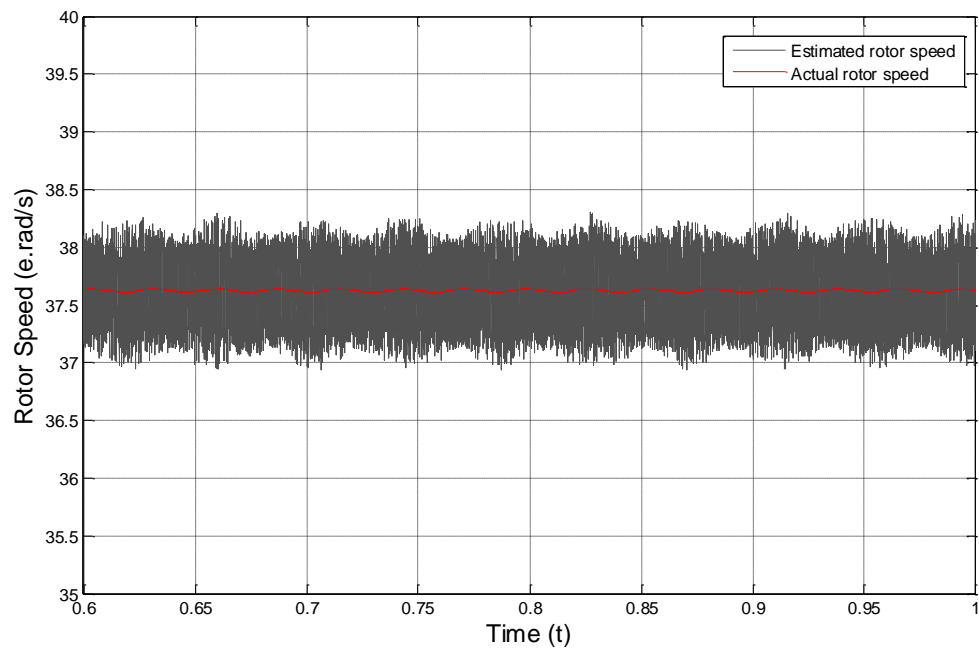


Figure 5.5 Estimated and actual rotor speed (wind speed=8m/s)

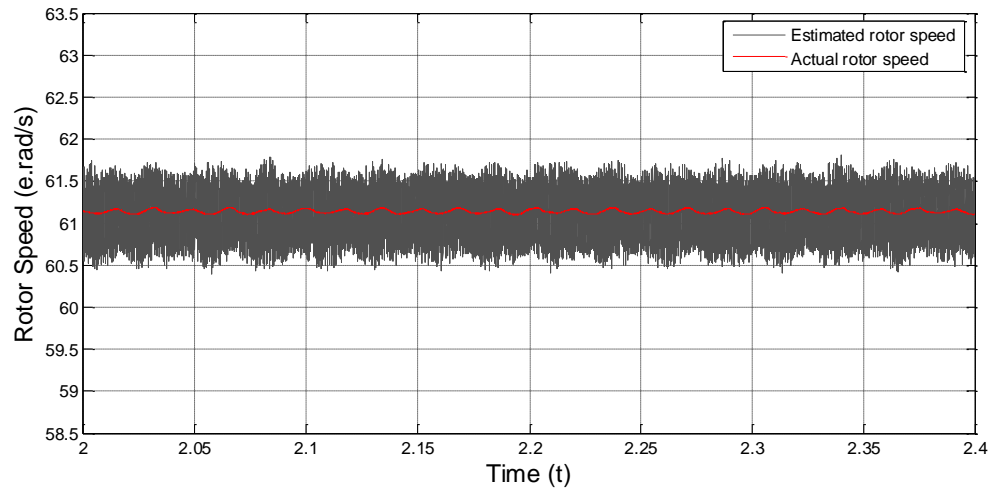


Figure 5.6 Estimated and actual rotor speed (wind speed=13m/s)

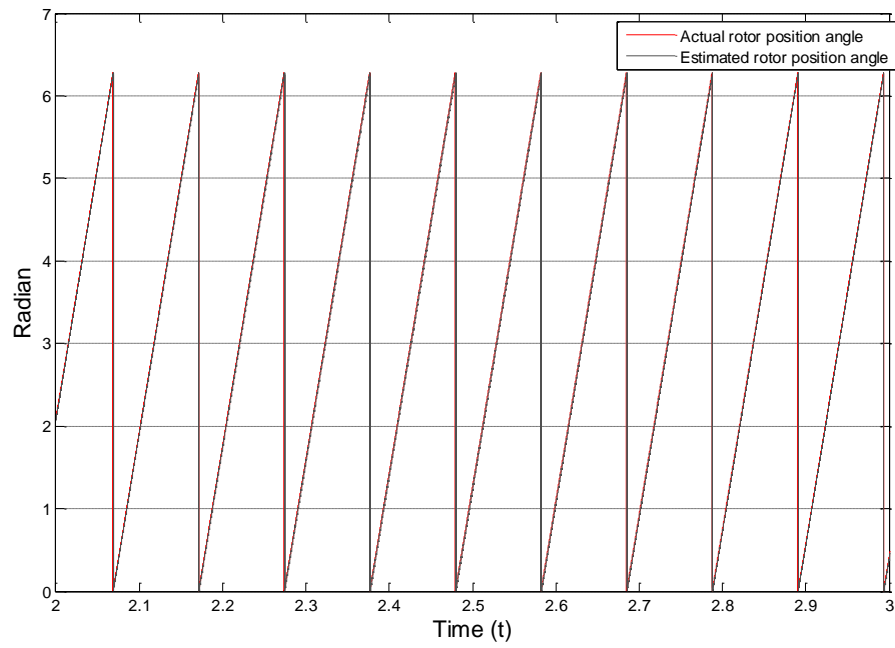


Figure 5.7 Estimated and actual rotor position angle

Figure 5.4 shows the simulation results of the estimated and actual rotor angular speed of the PMSG in electrical radian per second. Shown in Figures 5.5 and 5.6 are the zoom-in waveforms of the estimated and actual rotor speed when the wind speed is 8m/s and 13m/s (rated wind speed), respectively. As can be seen in these figures, the estimated values of the rotor speed correlate well to the actual rotor speeds, they almost overlap with each other. The band shape estimated rotor speed profile is due to the chattering effect of the SMO which has been introduced earlier.

Figure 5.7 shows the estimated and actual rotor position angle. From this figure, the estimated rotor position angle correlates well to the actual rotor position value. Again, the band shape estimated rotor position angle is due to the chattering effect of the sliding mode observer.

Based on the simulation results and the analysis, the proposed sliding mode observer based rotor speed and position sensorless control algorithm has been validated.

Chapter 6: Conclusions and Future Work

6.1 Conclusions

In this thesis, several important control algorithms for the wind turbine PMSG systems were studied and analyzed. In order to further validate the control methods, the control algorithms were applied to a case study 2 MW wind turbine PMSG system and a simulation study was performed in this thesis.

For the generator-side converter control, the optimal tip-speed ratio based MPPT control algorithm and vector control method were applied. From the simulation results, the MPPT method has shown the capability of controlling the wind turbine PMSG to generate the maximum power at different wind speeds. In addition, the high dynamic performance of the vector control method was also indicated in the simulation results, that is, when the wind speed changed, the generator speed which was controlled by the vector control algorithm reacted to the wind speed change very fast. Thus, for the wind turbine PMSG systems require high dynamic performance and high power capture efficiency, the optimal tip-speed ratio based MPPT control and vector control algorithms are qualified candidates.

For the grid-side converter control, the voltage oriented control algorithm was applied in this case study. By decoupling the active and reactive power components of the grid current, the voltage oriented control algorithm has the capability to control the active power and reactive power injected into the grid easily with high dynamic

performance. Thus, for the wind generation systems need to output the power with controllable power factor, the voltage oriented control method is a ideal selection.

In order to eliminate the PMSG rotor shaft sensor which would increase the hardware complexity as well as the cost of the system, a sliding mode observer based PMSG rotor position and speed self-sensing control was applied in this system. The simulation results indicated that the estimated rotor position and speed correspond to their actual values well. However, the chattering effect will increase the torque ripples of the PMSG and bring additional mechanical stress on the rotor shaft.

6.2 Future Work

In this thesis, a simulation study was carried out to validate the proposed control algorithms for a 2 MW wind turbine PMSG system. In order to further test the performance of the control algorithms, an experimental test needs to be done in the future research work. What is more, for the chattering effect of the sliding mode observer, effective mitigation methods need to be studied to alleviate the unwelcome effects brought by the chattering effect.

REFERENCES

- [1] R. W. Kates, "Climate change 1995: impacts, adaptations, and mitigation." *Environment: Science and Policy for Sustainable Development* 39.9 (1997): 29-33.
- [2] S. R. Bull, "Renewable energy today and tomorrow," *proc. IEEE*, vol. 89, no. 8, pp. 1216-1226, Aug. 2001.
- [3] "Technology opportunities to reduce U.S. greenhouse gas emissions," National Laboratory Directors, available: http://www.ornl.gov/climate_change/climate.htm, 1997.
- [4] T. Burton, N. Jenkins, D. Sharpe, and E. Bossanyi, *Wind energy handbook*. Wiley, 2011.
- [5] N. Hodge, "The truth about energy," Available: <http://www.energyandcapital.com/articles/the-truth-about-energy/2535>.
- [6] B. Wu, Y. Lang, N. Zargari, and S. Kouro, *Power Conversion and Control of Wind Energy Systems*. Hoboken, NJ: Wiley, 2011.
- [7] J. Ribrant and L. M. Bertling, "Survey of failures in wind power systems with focus on Swedish wind power plants during 1997–2005," *IEEE Trans. Energy Convers.*, vol. 22, no. 1, pp. 167–173, Mar. 2007.
- [8] F. Blaabjerg, M. Liserre, and K. Ma, "Power electronics converters for wind turbine systems," *IEEE Transactions on Industry Applications*, vol. 48, no. 2, pp. 708-719, 2012.
- [9] M. Liserre, R. Cardenas, M. Molinas, and J. Rodriguez, "Overview of multi-MW wind turbines and wind parks," *IEEE Trans. on Ind. Electron.*, vol. 58, no. 4, pp. 1081–1095, Apr. 2011.
- [10] K. Samir, J. Rodriguez, B. Wu, S. Bernet, and M. Perez. "Powering the Future of Industry: High-Power Adjustable Speed Drive Topologies," *Industry Applications Magazine, IEEE*, vol. 18, no. 4 (2012): 26-39.
- [11] J. Rodríguez, S. Bernet, B. Wu, J. O. Pontt, and S. Kouro. "Multilevel voltage-source-converter topologies for industrial medium-voltage drives," *IEEE Transactions on Industrial Electronics*, vol. 54, no. 6, pp. 2930-2945, 2007.
- [12] A. Nabae, I. Takahashi, and H. Akagi, "A new neutral-point-clamped PWM inverter," *IEEE Trans. Ind. Appl.*, vol. IA-17, no. 5, pp. 518–523, 1981.
- [13] R. H. Baker, "Bridge converter circuit," U.S. Patent 4 270 163, May 26, 1981.

- [14] T. Brückner, S. Bernet, and H. Güldner, "The active NPC converter and its loss-balancing control," *IEEE Trans. Ind. Electron.*, vol. 52, no. 3, pp. 855–868, Jun. 2005.
- [15] W. McMurray, "Fast response stepped-wave switching power converter circuit," U.S. Patent 3 581 212, May 25, 1971.
- [16] P. W. Hammond, "A new approach to enhance power quality for medium voltage ac drives." *IEEE Transactions on Industry Applications*, vol. 33, no. 1, pp. 202-208, 2007.
- [17] Wu, Bin. High-power converters and AC drives. Wiley-IEEE Press, 2006.
- [18] P. L. Jansen, R. D. Lorenz, "Transducerless Field Orientation Concepts Employing Saturation-Induced Saliencies in Induction Machines," *IEEE Transactions on Industry Applications*, vol. 32, no. 6, pp. 1380-1393, 1996.
- [19] M. J. Coney, R. D. Lorenz, "Rotor Position and Velocity Estimation for a Permanent Magnet Synchronous Machine at Standstill and High Speeds," *IEEE Transaction on Industry Applications*, vol. 34, no. 4, pp. 784-789.
- [20] R. C. Becerra, T. M. Jahns, and M. Ehsani, "Four-quadrant sensorless brushless ECM drive," *IEEE Conference Proceedings in Applied Power Electronics Conference and Exposition*, 1991, pp. 202-209, 1991.
- [21] R. Wu, and R. S. Gordon, "A permanent magnet motor drive without a shaft sensor." *Industry Applications*, *IEEE Transactions on Industry Applications*, vol. 27, no. 5, pp. 1005-1011, 1991.
- [22] M. C. Huang, A. J. Moses, and F. Anayi, "The comparison of sensorless estimation techniques for PMSM between extended Kalman filter and flux-linkage observer," *IEEE Conference and Exposition In Applied Power Electronics*, 2006, pp. 6-pp 2006.
- [23] T. Senjyu, T. Shimabukuro, and K. Uezato, "Vector control of permanent magnet synchronous motors without position and speed sensors," *IEEE Power Electronics Specialists Conference*, vol. 2, pp. 759-765, 1995.
- [24] M. Fu and L. Xu, "A Novel Sensorless Control Technique for Permanent Magnet Synchronous Motor (PMSM) Using Digital Signal Processor (DSP)" *IEEE Aerospace and Electronics Conference*, vol. 1, pp. 403~408, 1997.
- [25] C. French, P. Acarnley, "Control of Permanent Magnet Motor Drives Using a New Position Estimation Technique," *IEEE Transactions on Industry Applications*, vol. 32, no. 5, pp. 1089-1097, 1996.
- [26] Senjyu T, Shimabukuro T, Uezato K. Vector Control of Permanent Magnet Synchronous Motors Without Position and Speed Sensors [C]. *IEEE PESC Record*, 1995, (2) : 759-765.
- [27] K. David Young, V. I. Utkin, and U. Ozguner, "A control engineer's guide to sliding mode control," *IEEE Trans. on Control System Technology*, vol. 7, no. 3, pp. 328-342, 1999.

- [28] C. Edwards and S. K. Spurgeon, "Sliding Mode Control: Theory and applications," New York: Taylor & Francis, 1998.
- [29] V. I. Utkin, "Sliding mode control design principles and applications to electric drives," IEEE Trans. Ind. Electron., vol. 40, no. 1, pp. 23-36, 1993
- [30] V. I. Utkin, "Sliding mode and their application in variable structure systems," MIR Publishers, Moscow, 1974.
- [31] K. Kang, J. Kim, K. B. Hwang, and K. H. Kim, "Sensorless control of PMSM in high speed range with iterative sliding mode observer," in Conf. Rec. IEEE APEC, vol. 2, pp. 1111-1116, 2004.
- [32] A. Sabanovic and F. Bilalovic, "Sliding mode control of AC drives," IEEE Trans. Ind. Applicat., vol. 25, pp. 70-75, 1989.
- [33] Z. Yan and V. Utkin, "Sliding mode observers for electric machines-An overview," in Proc. 28th IEEE IECON, Nov. 2002, vol. 3, pp. 1843-1847.
- [34] H. Kim, J. Son, and J. Lee, "A high-speed sliding-mode observer for the sensorless speed control of a PMSM," IEEE Trans. Ind. Electron., vol. 58, no. 9, pp. 4069-4077, 2011.
- [35] R. A. DeCarlo, S. H. Zak, and G. P. Matthews, "Variable structure control of nonlinear multivariable systems: A tutorial," Proc. IEEE, vol. 76, pp. 212-232, 1988.
- [36] S. Chi, Z. Zhang, and L. Xu, Sliding-Mode Sensorless Control of Direct-Drive PM Synchronous Motors for Washing Machine Applications, IEEE Trans. on Industry Applications, Vol. 45, No. 2, pp. 582-590, 2009.
- [37] W. Qiao, X. Yang, and X. Gong, "Wind Speed and Rotor Position Sensorless Control for Direct-Drive PMG Wind Turbines," IEEE Transactions on Industry Applications, Vol. 48, No. 1, pp. 3-11, 2012.
- [38] Betz, Albert. "Behavior of vortex systems." (1933).
- [39] "WE Handbook-2-Aerodynamics and Loads", available: <http://www.gurit.com>
- [40] M. Singh, *Adaptive Network-Based Fuzzy Inference Systems for Sensorless Control of PMSG Based Wind Turbine With Power Quality Improvement Features*. (Doctoral dissertation). Retrieved from ProQuest Dissertation and Thesis.
- [41] A. E. Fitzgerald, J. C. Kingsley, and S. D. Umans, *Electric Machinery*. New York: McGraw-Hill, 1990.
- [42] R. M. Park, "Two-reaction theory of synchronous machines, pt. I: Generalized method of analysis," AIEE Trans., vol. 48, pp. 716-730, July 1929.
- [43] I. Takahashi and Y. Ohmori, "High-performance direct torque control of an induction motor," IEEE Trans. Ind. Applicat., vol. 25, pp. 257-264, 1989.

- [44] Blaschke, Felix. "The principle of field orientation as applied to the new TRANSVECTOR closed loop control system for rotating field machines." *Siemens review* 34, no. 5 (1972): 217-220.
- [45] Holmes, D. Grahame, and Thomas A. Lipo. *Pulse width modulation for power converters: principles and practice*. Vol. 18. Wiley-IEEE Press, 2003.
- [46] Van Der Broeck, Heinz Willi, H-C. Skudelny, and Georg Viktor Stanke. "Analysis and realization of a pulsewidth modulator based on voltage space vectors." *Industry Applications, IEEE Transactions on* 24, no. 1 (1988): 142-150.
- [47] J. Shao, D. Nolan, and T. Hopkins, "A Novel Direct Back EMF Detection for Sensorless Brushless DC (BLDC) Motor Drives," in *Proc. IEEE APEC*, vol. 1, pp.33-37, 2002.
- [48] T. Sun, Z. Chen, and F. Blaabjerg, "Voltage Recovery of Grid-Connected Wind Turbines After a Short-Circuit Fault," *Proc. of the 29th Annual Conference of the IEEE Industrial Electronics Society*, vol. 3, June 20-25, 2004, pp. 827-831.